The Presence of the Temporal Horn Exacerbates the Vulnerability of Hippocampus during Head Impacts

Authors

Zhou Zhou,[1,2†*] Xiaogai Li, [2†] August G Domel,[1] Emily L Dennis,[3,4] Marios Georgiadis,[4] Yuzhe Liu,[1] Samuel J. Raymond,[1] Gerald Grant,[4,5] Svein Kleiven,[2‡] David Camarillo,[1,5,7‡] Michael Zeineh[4‡*]

Affiliations

[1] Department of Bioengineering, Stanford University, Stanford, CA, 94305, USA.

[2] Neuronic Engineering, KTH Royal Institute of Technology, Stockholm, 14152, Sweden.

[3] TBI and Concussion Center, Department of Neurology, University of Utah, Salt Lake City, 84108, USA

[4] Department of Radiology, Stanford University, Stanford, CA, 94305, USA.

[5] Department of Neurosurgery, Stanford University, Stanford, CA, 94305, USA.

[6] Department of Neurology, Stanford University, Stanford, CA, 94305, USA.

[7] Department of Mechanical Engineering, Stanford University, Stanford, CA, 94305, USA.

[*] Corresponding author. Email: zhouz@stanford.edu, mzeineh@stanford.edu

[†] These authors contributed equally to this work.

[‡] These authors share senior authorship.

Corresponding authors

Zhou Zhou, Department of Bioengineering, Stanford University, Stanford, CA, 94305, USA, Email:zhouz@stanford.edu

Michael Zeineh, Department of Radiology, Stanford University, 213 Quarry Road, Stanford, CA 94305, USA, Email: mzeineh@stanford.edu

Other authors

Xiaogai Li, Division of Neuronic Engineering, Royal Institute of Technology (KTH), SE-14152, Huddinge, Sweden, Email: xiaogai@kth.se

August G Domel, Department of Bioengineering, Stanford University, Stanford, CA, 94305, USA, Email: augustdomel@gmail.com

Emily L Dennis, TBI and Concussion Center, Department of Neurology, University of Utah, Salt Lake City, 84108, USA, Email: eldennis@stanford.edu

Marios Georgiadis, Department of Radiology, Stanford University, 213 Quarry Road, Stanford, CA 94305, USA, Email: mariosg@stanford.edu

Yuzhe Liu, Department of Bioengineering, Stanford University, Stanford, CA, 94305, USA, Email: yuzheliu@stanford.edu

Samuel J. Raymond, Department of Bioengineering, Stanford University, Stanford, CA, 94305, USA, Email: sjray@stanford.edu

Gerald Grant, Department of Neurosurgery, Stanford University School of Medicine, 291 Campus Drive, Stanford, CA 94305, Stanford, CA. Email: ggrant2@stanford.edu

Svein Kleiven, Division of Neuronic Engineering, Royal Institute of Technology (KTH), SE-14152, Huddinge, Sweden, Email: sveink@kth.se

David Camarillo, Department of Bioengineering, Stanford University, 443 Via Ortega, Room 202, Stanford, CA, 94305, Email: dcamarillo@stanford.edu

Abstract

Hippocampal injury is common in traumatic brain injury (TBI) patients, but the underlying pathogenesis remains elusive. In this study, we hypothesize that the presence of the adjacent fluid-containing temporal horn exacerbates the biomechanical vulnerability of the hippocampus. Two finite element models of the human head were used to investigate this hypothesis, one with and one without the temporal horn, and both including a detailed hippocampal subfield delineation. A fluid-structure interaction coupling approach was used to simulate the brain-ventricle interface, in which the intraventricular cerebrospinal fluid was represented by an arbitrary Lagrangian-Eulerian multi-material formation to account for its fluid behavior. By comparing the response of these two models under identical loadings, the model that included the temporal horn predicted increased magnitudes of strain and strain rate in the hippocampus with respect to its counterpart without the temporal horn. This specifically affected cornu ammonis (CA) 1 (CA1), CA2/3, hippocampal tail, subiculum, and the adjacent amygdala and ventral diencephalon. These computational results suggest the presence of the temporal horn is a predisposing factor for the prevalence of hippocampal injury, advancing the understanding of hippocampal injury during head impacts. A corresponding analysis in an imaging cohort of collegiate athletes found that temporal horn size negatively correlates with hippocampal volume in the same subfields, suggesting a possible real-world correlation whereby a larger temporal horn may be associated with decreased hippocampal volume. Our biomechanical and neuroimaging effort collectively highlight the mechanobiological and anatomical interdependency between the hippocampus and temporal horn.

Keywords

2

Introduction

Traumatic brain injury (TBI) is a critical public health and socio-economic problem. In the United States, approximately 5.3 million people are living with a TBI-related disability (Langlois and Sattin, 2005). At a global level, an estimated 69 million people suffer a TBI each year (Dewan et al., 2018), with yearly costs reaching 400 billion dollars (Maas et al., 2017). Despite worldwide efforts to reduce the incidence and mitigate the consequence of TBI, improvement of overall outcome has not been achieved (Roozenbeek et al., 2013), especially for mild TBI (mTBI), also known as concussion. Epidemiological data showed that concussion rates in high school sports (Rosenthal et al., 2014) and the military (Cameron et al., 2012) have been rising. The need to improve concussion outcome is particularly urgent, given that concussion is notoriously underreported, difficult to screen, and associated with immediate and persistent deficit to memory and attention with possible chronic neurodegenerative consequences (McKee et al., 2015;Meier et al., 2015).

As a crucial structure for long-term, episodic memory formation and retrieval (Bird and Burgess, 2008), the hippocampus is often reported to be injured secondary to physical trauma in humans across different impact severities. In fatal TBI, post-mortem histopathological examinations identify the hippocampus as one of the most commonly injured regions (73%-87%) (Kotapka et al., 1992;Kotapka et al., 1993;Kotapka et al., 1994;Maxwell et al., 2003). In mTBI, *in vivo* human imaging analyses demonstrate that repetitive concussive impacts or even sub-concussive impacts (i.e., high-velocity impacts that do not cause concussion) are associated with abnormal hippocampal atrophy longitudinally (Parivash et al., 2019) and cross-sectionally (Singh et al., 2014). The prevalence of hippocampal injury has also been widely noted in animal experiments (e.g., non-human primates, pigs, rats, sheep, and rabbits) under diverse modes of mechanical perturbations, including non-impact acceleration (Gennarelli et al., 1982;Kotapka et al., 1991), impact acceleration (Anderson et al., 2003), weight-drops (Kalish and Whalen, 2016),

3

93   cortical contusion (Baldwin et al., 1997), and fluid percussion injury (Hicks et al., 1996). The

94   resultant injury within the hippocampus of experimentally traumatized animals exhibits a broad

95   spectrum of pathological manifestations, varying from impaired electrophysiological activity

96   associated with hippocampal circuitry dysfunction (Wolf et al., 2017) to profound neuronal

97   apoptosis and marked gliosis (Smith et al., 1997).

98   The pathogenetic mechanism of trauma-induced hippocampal injury has long been

99   attributed to the selective vulnerability of hippocampal neurons to hypoxemia and ischemia

100 (Pulsinelli, 1985;Ng et al., 1989), typical complications of severe TBI insults (Graham et al.,

101 1978;Graham et al., 1989). For example, a histopathological study revealed that 27 out of 29

102 individuals with at least one episode of clinically recorded hypoxia had hippocampal damage

103 (Kotapka et al., 1992). However, 14 out of 18 patients without documented hypoxemia also had

104 hippocampal lesions (Kotapka et al., 1992), suggesting that hippocampal injury may be independent

105 of hypoxia. Another candidate mechanism is pathological neuronal excitation involving glutamate

106 and/or other excitatory amino acid neurotransmitters, supported by animal experiments where

107 traumatic insults triggered glutamate concentrations in the extracellular fluid of the hippocampus

108 (Faden et al., 1989;Runnerstam et al., 2001). Given that the hippocampus is dense in receptors for

109 glutamate (Kotapka et al., 1991;Leranth et al., 1996), redundant extracellular glutamate could

110 induce neuronal excitotoxicity, and indeed, pre-treatment of experimentally traumatized animals

111 with glutamate antagonists attenuates hippocampal lesions (Faden et al., 1989). However, such

112 antagonists in humans have not proven beneficial, thus, a neuroexcitotoxic mechanism in human

113 TBI cannot be considered a sole explanation (Parsons et al., 1999). Taken together, trauma-induced

114 hippocampal lesions in humans cannot be fully explained by the current mechanisms.

115   An alternative line of investigation is biomechanical. Given that previous modeling work

116 has shown that the presence of fluid can affect the transmission of mechanical forces within the

117 brain (Zhou et al., 2020a), one structure that may be associated with the hippocampal vulnerability

4

118   is the temporal horn of the lateral ventricle. The temporal horn is a cavity that forms the roof of the

119   hippocampus and is filled with cerebrospinal fluid (CSF) and occasionally choroid plexus (Insausti

120   and Amaral, 2003). Previous studies found that the volumes of the hippocampus and temporal horn

121   were inversely correlated in TBI patients (Gale et al., 1994;Bigler et al., 1997;Bigler et al., 2002).

122   This has largely been surmised to be secondary to volume loss, but this oversimplification can miss

123   a potentially important pathology-induced volumetric interdependency. To date, the biomechanical

124   effect of the temporal horn on the hippocampus remains unknown.

125   Interrogation of this biomechanical relationship requires modeling to estimate the myriad

126   variables and forces at play. As computational surrogates of the human head, finite element (FE)

127   models have been instrumental in exploring the association of regional vulnerabilities with potential

128   predisposing factors during trauma from the biomechanical perspective (Kleiven, 2007;McAllister

129   et al., 2012;Mao et al., 2013;Ji et al., 2015;Atsumi et al., 2018;Trotta et al., 2020;Zhou et al., 2021a).

130   Extending the current models to investigate the relationship between the temporal horn and

131   hippocampus requires that the FE model possesses an anatomically and mechanically accurate

132   representation of both structures, and a precise description of the interface between the fluid-filled

133   temporal horn and neighboring hippocampus. However, in existing finite element models, the

134   temporal horn was either wholly substituted as brain parenchyma (McAllister et al., 2012;Zhou et

135   al., 2016) or simulated as a solid structure using the Lagrangian approach (Kleiven, 2007;Mao et

136   al., 2013;Ji et al., 2015;Atsumi et al., 2018;Trotta et al., 2020;Zhou et al., 2021a). This Lagrangian

137   approach is a dominant numerical scheme for solid mechanics and is insufficient to computationally

138   reflect the fact that the temporal horn is filled with CSF with the potential flow within the ventricular

139   cavity during the impacts (Souli et al., 2000;Zhou, 2019;Zhou et al., 2020b). Approaches to date

140   may have missed key and relevant properties of the temporal horn that have precluded the

141   determination of its biomechanical relevance.

142 The primary aim of the current study was to discern whether the presence of the temporal

143 horn exacerbates the biomechanical vulnerability of the hippocampus. To test this hypothesis, two

144 models with and without a detailed anatomic description of the temporal horn profiles are

145 established. By comparing the strain-related responses to identical loadings between the two models,

146 the biomechanical mechanism for the temporal horn's role in the vulnerability of the hippocampus

147 was uncovered. In addition, we also analyzed neuroimaging data of male collegiate athletes to

148 investigate the volumetric interrelationship between the hippocampus and temporal horn.

Materials and Methods

150 In this study, we collectively employed computational modeling and neuroimaging analysis

151 to discern the biomechanical and volumetric interdependency between the hippocampus and

152 temporal horn. To achieve that, we utilized a novel, multi-million element 3D head model (Zhou et

153 al., 2020a) that did not initially incorporate the temporal horn (no-temporal-horn (NTH)-model),

154 and further extended this model by adding the temporal horn to the lateral ventricle (temporal-horn

155 (TH)-Model). An arbitrary Lagrangian-Eulerian (ALE) multi-material formation was used to

156 emulate the fluid behavior of the intraventricular CSF, with its responses being concatenated with

157 the brain tissue via a fluid-structure interaction (FSI) coupling algorithm. This allows computation

158 of strain (fractional change in unit length), strain rate (strain change over time), and stress (force

159 per unit area) in the hippocampus. By comparing the deformation-related responses estimated by

160 these two models secondary to six concussive/sub-concussive impacts, the mechanical role that the

161 temporal horn exerted on the hippocampus was revealed. To see if the modeled relationship

162 between the presence of the temporal horn and associated increased strains/strain rates had an in

163 vivo correlation, we analyzed data collected from 91 male collegiate athletes to evaluate the

164 volumetric relationship between the hippocampus and temporal horn.

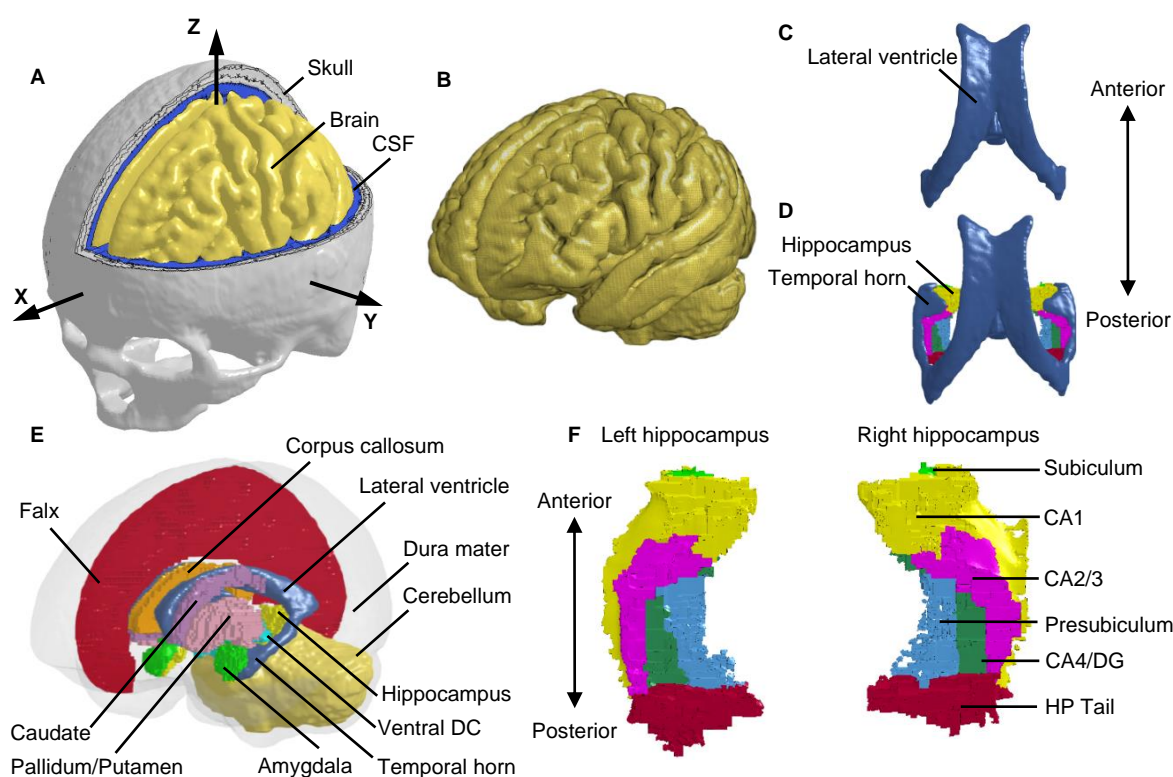### Finite element modeling of human brain

166 The FE head model without the temporal horn (i.e., the NTH-Model) used in this study was

167 previously developed at KTH Royal Institute of Technology in Stockholm, Sweden (Zhou et al.,

6

168   2020a). The model includes the scalp, skull, brain, subarachnoid CSF (i.e., CSF within the

169   subarachnoid space), meninges (i.e., dura mater and pia mater), falx, tentorium, and cerebral

170   ventricles (i.e., lateral ventricles without the temporal horn, and third ventricle) (Fig. 1). The whole

171   head model consists of 4.2 million hexahedral elements and 0.5 million quadrilateral elements, in

172   which the brain has a total of 2.6 million nodes, and 2.3 million hexahedral elements. The average

173   brain element size is 0.59 ± 0.26 mm, meeting the requirement that a human brain model with

174   converged responses should have an average element size less than 1.8 mm (Zhao and Ji, 2019).

175   Information regarding the geometry profiles and material modeling of various intracranial

176   components in the NTH-Model was elaborated in a previous study (Zhou et al., 2020a) as well as

177   in Appendix A.

178   To investigate the potential effect of the presence of the CSF-filled temporal horn on the

179   hippocampus, we extended the NTH-model by adding the fluid-filled temporal horn to the cerebral

180   ventricle (i.e., from Fig. 1C to Fig. 1D). This extended model (i.e., the TH-Model) has the same

181   geometrical features, material properties, element formulation, and interface conditions as the

182   NTH-Model, except for the newly added temporal horn. The volume ratio between the temporal

183   horn and the brain in the TH-Model was 0.13%, falling within the range in healthy adults (0.1%-

184   0.3%) (Bigler and Tate, 2001). Strain response and brain-skull relative motion estimated by the TH-

185   Model were respectively evaluated by the experiments presented by Hardy et al. (2007) and Zhou

186   et al. (2019c) in Appendix B. Details about the cerebral ventricle modeling and the brain-ventricle

187   interface of the TH-Model are elaborated in the following two sections, along with that in the NTH-

188   Model.

189   To facilitate the derivation of deformation-related metrics in regions of interest (ROIs) from

190   completed simulations, the brain segmentation was registered to the coordinate system of the FE

191   head model and then the brain elements were grouped into different sub-regions according to the

192   spatial correspondence with the brain segmentation via an automated procedure implemented by a

7

193 custom-built MATLAB script. For both the TH-Model and NTH-Model, the anatomically classified

194 brain regions included cerebral cortex, cerebellum, hippocampus with six subfields as segmented

195 by FreeSurfer 7 (i.e., cornu ammonis (CA) 1, CA2/3, CA4/dentate gyrus (DG), hippocampus tail

196 (HP Tail), subiculum, and presubiculum) (Fig. 1F), and non-hippocampal paraventricular regions

197 (i.e., amygdala, ventral diencephalon (ventral DC), pallidum, putamen, caudate, and corpus

198 callosum (CC)) (Fig. 1E).

199
200 **Fig. 1. Finite element models of the human head with and without the temporal horn.** (**A**)
201 Head model with the skull open to expose the subarachnoid CSF and brain. A skull-fixed coordinate
202 system and corresponding axes are illustrated with the origin at the center of gravity of the head.
203 (**B**) Brain model with fine mesh. (**C**) Ventricles (i.e., lateral ventricles without the temporal horn,
204 and third ventricle) in the NTH-model. (**D**) Ventricles (i.e., lateral ventricles with the temporal horn,
205 and third ventricle) in the TH-model and hippocampus. (**E**) Isometric view of deep brain structures,
206 cerebral ventricles, falx, and dura mater (in translucency) in the TH-Model. (**F**) Left and right
207 hippocampal formations with subfields. CSF: cerebrospinal fluid; Ventral DC: ventral
208 diencephalon; CA: cornu ammonis; DG: dentate gyrus; HP Tail: hippocampal tail.

Cerebral ventricle modeling

210   To emulate the fluid properties of the intraventricular CSF and potential CSF flow

211 secondary to exterior loading, the cerebral ventricles in the TH-Model (Fig. 2A) and NTH-Model

212 (Fig. 2B) were simulated using an ALE multi-material formulation. This formulation advances the

8

213 solution in time using a two-step operation, in which the material is antecedently deformed in a

214 Lagrangian step and subsequently followed by an advection step with the element variables being

215 remapped (Zhou et al., 2019b). In the Lagrangian step, the intraventricular CSF deformation was

216 determined by the equation of state (for dilatational responses) and constitutive equation (for

217 deviatoric responses) listed in Table 1, together with associated formulations and material constants.

218 In the advection step, a second-order van Leer scheme was selected, excelling in advection accuracy

219 and numerical stability (van Leer, 1979).

220 **Table 1. Material constant for the cerebral ventricles in the TH-Model and NTH-Model.** P:
221 pressure, C: intercept of $v_s - v_p$ curves, v_s: velocity of a shockwave traveling through the
222 intermediary material, v_p: velocity of the shocked material; S_1, S_2, and S_3: coefficients of the slope
223 of the $v_s - v_p$ curves, γ_0: Gruneisen gamma, a: first order volume correction to γ_0; ρ_0: initial
224 density; ρ: instantaneous density; σ_{ij}^v: deviatoric stress; γ: dynamic viscosity; $\dot{\varepsilon}_{ij}^{'}$: deviatoric
225 strain rate; PC: cut-off pressure.

Equation of state	ρ_0 (kg/m3)	C (m/s)	S_1	S_2	S_3	a	γ_0
$P = \dfrac{\rho_0 C^2 \mu (1 + (1 - \frac{\gamma_0}{2})\mu - \frac{a}{2}\mu^2}{[1 - (S_1 - 1)\mu - S_2 \frac{\mu^2}{\mu+1} - S_3 \frac{\mu^3}{(\mu+1)^2}]}; \mu = \dfrac{\rho}{\rho_0} - 1$	1000	1482.9	2.10	-0.17	0.01	0	1.2
Constitutive equation	γ (Pa.s)	PC (MPa)					
$\sigma_{ij}^v = \gamma \dot{\varepsilon}_{ij}^{'}$	0.001	-22					

226 **Brain-ventricle interface modeling**

227 To couple the mechanical responses of the ALE-represented intraventricular CSF with the

228 Lagrangian-represented brain, a penalty-based FSI coupling scheme (Batterbee et al., 2011;Zhou et

229 al., 2019a) was implemented to both the TH-Model and NTH-Model. The implemented coupling

230 scheme delivers tension and compression in the radial direction and allows relative motion in the

231 tangential direction.

232 Owing to the requirement of implementing the penalty-based coupling scheme, any

233 locations to which the fluid may potentially flow during the simulations are required to be meshed.

234 Considering that the intraventricular CSF might flow to regions that were originally occupied by

235 deep brain structures (due to deformation of the brain itself and the relative motion between the

9

236 brain and cerebral ventricles during the simulation), additional meshes were generated in these

237 regions, referred to as the "void mesh" in Fig. 2A and Fig. 2B, and initially overlapped with part of

238 the brain elements. The void mesh was emulated with the ALE multi-material element approach,

239 with material properties identical to that of the intraventricular CSF (Table 1) along with an extra

240 void definition. Such a void definition ensured that no fluid was distributed within the void mesh

241 under its initial configuration. The motion of the ALE elements followed the mass-weighted

242 velocity in the ALE mesh (Hallquist, 2007).
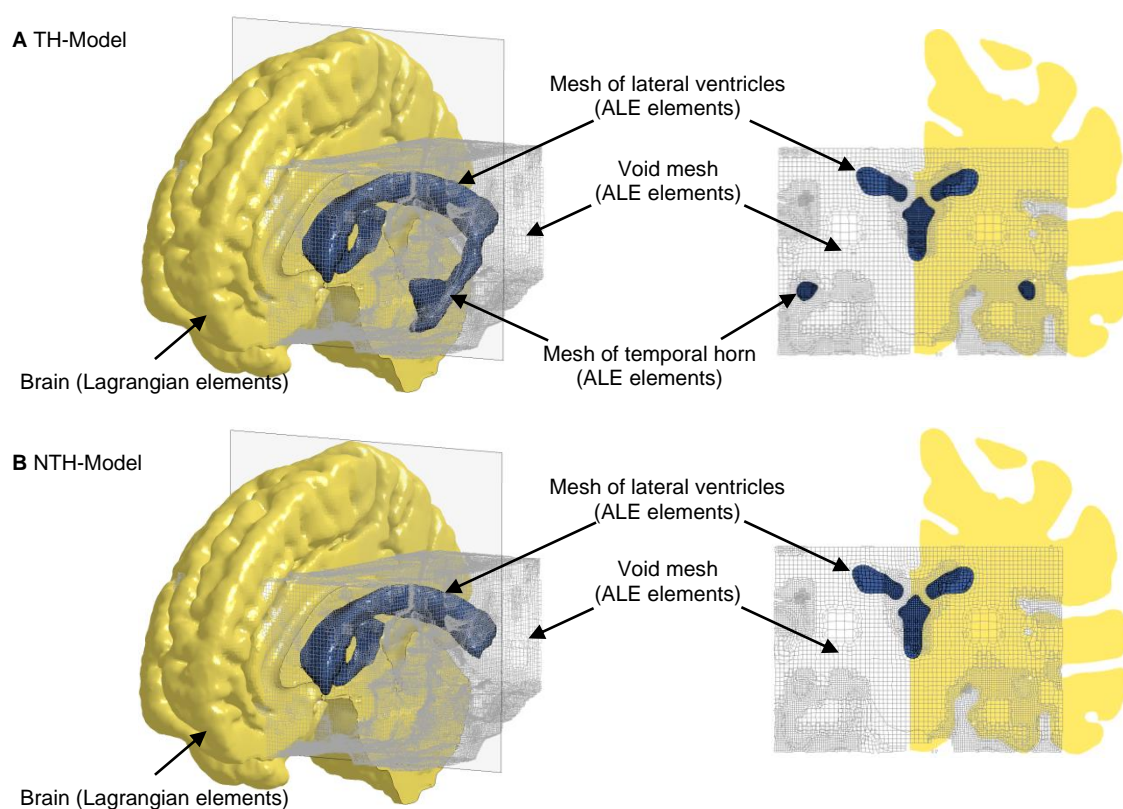
Fig 2. Brain-ventricle interfaces of the TH-Model (A) and NTH-Model (B). For each model, an isometric view of the brain model, the cerebral ventricle, and void mesh are shown on the left. Coronal sections at the planes indicated in the left subfigures are shown on the right. For better illustration, only half of the brain is visible. The cerebral ventricles are shown as blue shaded elements and the void mesh as wireframe elements. ALE: arbitrary Lagrangian-Eulerian.

Loading conditions

250   Estimation of hippocampal response was obtained from the TH-Model and NTH-Model by

251 simulating 6 representative football head impacts (Table 2 and Appendix B). At Stanford University,

252 instrumented mouthguards have been developed to measure six-degree-of-freedom head kinematics

10

253 during in-game head impacts to athletes (Liu et al., 2020a;Cecchi et al., 2021). Using these

254 instrumented mouthguards, over 500 head impacts in football have been video confirmed

255 (Hernandez et al., 2015). In the current study, two concussive impacts, one with the athlete suffering

256 alteration of consciousness (Case 1) and the other with the player having a milder but self-reported

257 concussion (Case 2), and two sub-concussive impacts (Case 4 and Case 5) were simulated. In

258 addition, a helmet-to-helmet collision involving two players was simulated with the struck player

259 (Case 3) having a concussion and the striking player not (Case 6). Video recordings of the game

260 were analyzed, through which the initial head kinematics were determined and further guided the

261 laboratory reconstruction to obtain the dynamic kinematics of this collision (Pellman et al.,

262 2003;Sanchez et al., 2019). All simulations were solved by the massively parallel processing

263 version of LS-DYNA R11 double precision with 128 processors.

264 **Table 2. Peaks of translational acceleration and rotational acceleration and injury severity of**
265 **the 6 cases considered in this study.** The X, Y, and Z axes are the same as those in the skull-fixed
266 coordinate system in Fig. 1A. Note that Cases 1-2 and Cases 4-5 are on-filed impacts measured by
267 the mouthguard (Hernandez et al., 2015), while Case 3 and Case 6 are laboratory-reconstructed
268 impacts (Pellman et al., 2003;Sanchez et al., 2019).

Case ID	Peak translational acceleration (g)				Peak rotational acceleration (krad/s^2)				Injury severity
	X	Y	Z	Magnitude	X	Y	Z	Magnitude	
Case 1	-40.6	100.4	-63.4	106.1	12.89	-3.06	-3.24	12.95	Concussion
Case 2	-61.1	-57.8	-45.8	84.2	4.21	5.14	-1.84	6.19	Concussion
Case 3	-31.9	133.4	41.6	134.0	4.65	1.20	-6.81	7.50	Concussion
Case 4	-49.3	-47.2	-32.3	71.9	2.44	-4.36	-7.26	7.75	Sub-concussion
Case 5	7.3	18.1	11.4	20.4	4.12	0.59	1.05	4.14	Sub-concussion
Case 6	-21.5	-59.4	57.8	78.8	-5.82	-1.66	-2.44	6.24	Sub-concussion

269 The strain and strain rates in the 6 hippocampal subfields, the whole hippocampus, and 6

270 non-hippocampal periventricular regions were extracted from the two models, resulting in a total

271 of 13 region-wise comparisons for each injury metric. This was motivated by the findings that

272 hippocampal cell death was significantly affected by the strain (Cater et al., 2006) and hippocampal

273 functional impairment was dependent on both strain and strain rate (Kang and Morrison, 2015) in

274 *in vitro* TBI models on organotypic hippocampal slice cultures from rat. The strain was calculated

275 as the maximum principal value of the Green-Lagrange strain tensor, while the strain rate was

276 computed as the maximum principal value of rate of deformation tensor (Holzapfel, 2000). To

277 eliminate potential numerical artifacts, the 95th percentile maximum principal strain and the 95th

278 percentile maximum principal strain rate over the simulated time windows were presented for all

279 ROIs (Panzer et al., 2012;Zhou et al., 2021b).

Neuroimaging analysis

Study population and imaging acquisition

282   We sought to identify if the relationship between the presence of the temporal horn and

283 associated strains showed an imaging correlation, specifically if there was a volumetric relationship

284 between the hippocampus and temporal horn. For this, we analyzed data collected from 91 male

285 collegiate athletes (mean age (standard deviation): 19.3 (1.43) years). This was a new analysis of

286 previously collected and processed data (Parivash et al., 2019). All procedures were in accordance

287 with the Institutional Review Board of Stanford University School of Medicine and Health

288 Insurance Portability and Accountability. The enrolled subjects had no self-reported history of brain

289 surgery, severe brain injury, or major neurological, psychiatric, or substance abuse disorder. All

290 brain MRI datasets were scrutinized for abnormalities by a neuroradiologist to further exclude any

291 clinically evident brain injury.

Imaging acquisition

293   Standard protocols were used to acquire MRIs using a 3T magnetic resonance imaging

294 (MRI) scanner (GE MR 750, Milwaukee, WI, USA) and an 8-channel-receive head coil. For each

295 participant, we acquired T_1-weighted axial images (inversion recovery fast spoiled gradient echo

296 brain volume imaging, voxel size = $1 \times 1 \times 1$ mm^3, repetition time (TR) = 7.9 ms, echo time = 3.1

297 ms, number of excitations (NEX) = 1, acquisition time = 5.1 min) and high-resolution coronal T_2-

298 weighted images, perpendicular to the long axis of the hippocampus (coronal oblique fast spin echo,

299 voxel size = $0.29 \times 0.52 \times 2$ mm^3, 0.2 mm skip, TR= 5000-15000 ms, TE = 95-109 ms, echo train

300   length = 25, matrix = 512×384, NEX=2, 32-40 slices, one to two acquisitions, acquisition time =

301   4.4-5.8 min).

Segmentation

303   Images were segmented using Automated Segmentation of Hippocampal Subfields (ASHS)

304   (Contijoch et al., 2015), excelling in performing multi-atlas label fusion and machine-learning

305   correction to obtain reliable segmentation of the hippocampal subfields and adjacent structures (e.g.,

306   temporal horn as the ROI in the current study). In ASHS, the hippocampal subfields include CA1,

307   CA2-4, DG, subiculum, entorhinal cortex (ERC), and perirhinal cortex (PRC). Given that the CA4

308   and DG are inseparable on individual segmentations and CA2 and CA3 are small in size, subfields

309   CA2-4 and DG were combined into one subregion, referred to as CA2-4/DG. Similarly, ERC and

310   PRC were combined into one subregion (ERC/PRC). Automated segmentations for the

311   hippocampus and temporal horn were manually checked for accuracy by three independent, blinded

312   raters as previously described (Parivash et al., 2019). Subfield volumes were summed to obtain

313   total hippocampal volume. To regress out the inter-subject differences in head size (Barnes et al.,

314   2010), we measured the intracranial volume of all participants using the FreeSurfer software (Fischl,

315   2012).

Statistical analysis

317   For the computational simulations, percentage differences in the 95th percentile maximum

318   value of strain and strain rate predicted by the TH-Model and NTH-Model were computed at a

319   region-wise basis, with the value from the NTH-Model as reference. Thus, the 95th percentile

320   maximum values of strain and strain rate estimated by the TH-Model and NTH-Model were

321   respectively extracted from each loading case for a total of 13 ROIs, including 6 hippocampal

322   subfields, the whole hippocampus, and 6 non-hippocampal paraventricular regions. To statistically

323   ascertain the influence of temporal horn on the deformation-related responses, the strain and strain

324   rate in all 13 ROIs from the TH-Model and NTH-Model were analyzed with a Wilcoxon matched-

325   pairs signed-rank test, using an uncorrected significance threshold of $p<0.05$.

13

326   For the neuroimaging results, we examined the volumetric relationship between the

327   temporal horn and whole hippocampus, and each hippocampal subfield volume. Given that the

328   volumetric data for all ROIs exhibited normality, linear regression was used. We included total

329   intracranial volume in all regressions to reflect the volumetric dependencies of the hippocampus

330   and temporal horn on overall head size. The threshold for significance was $p < 0.05$, and multiple

331   comparison correction across subfields was performed with a threshold of 0.017 across the subfields

332   to account for covariance between the subfields (Li and Ji, 2005).

Results

Finite element modeling of human brain

Strain and strain rate in the hippocampus and adjacent structures

336   We first aimed at elucidating the changes in strain and strain rate distribution due to the

337   presence of the temporal horn. Cross-sections of whole-brain strain and strain rate maps are

338   presented in Fig. 3. Almost identical strain and strain rate patterns were predicted by these two

339   models, with the exception of strains exceeding 0.2 (Fig. 3A-B) and strain rates over 30 s^{-1} (Fig.

340   3C-D) around the temporal horn that was exclusively predicted by the TH-Model in all simulated
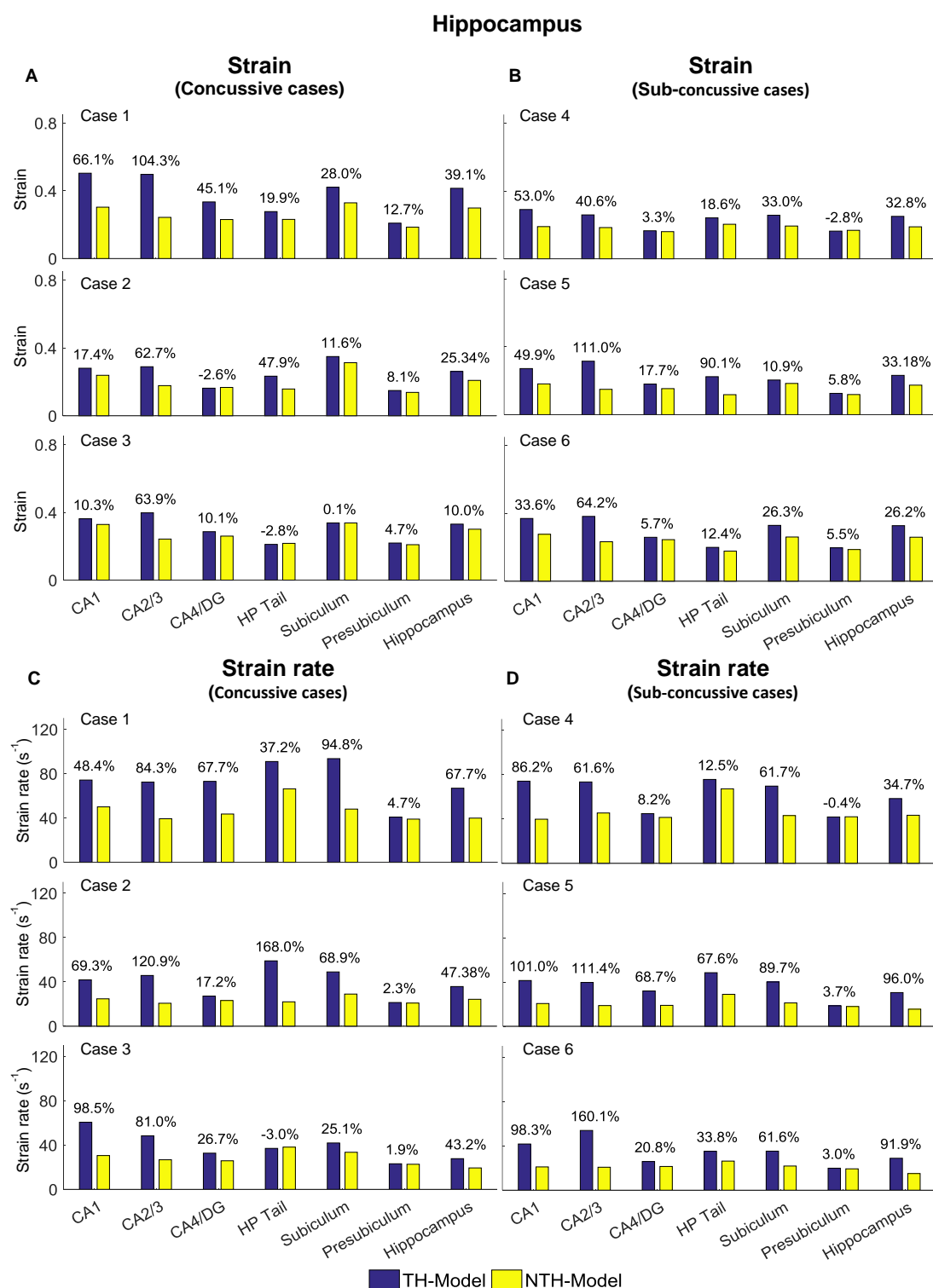
341   loading cases.
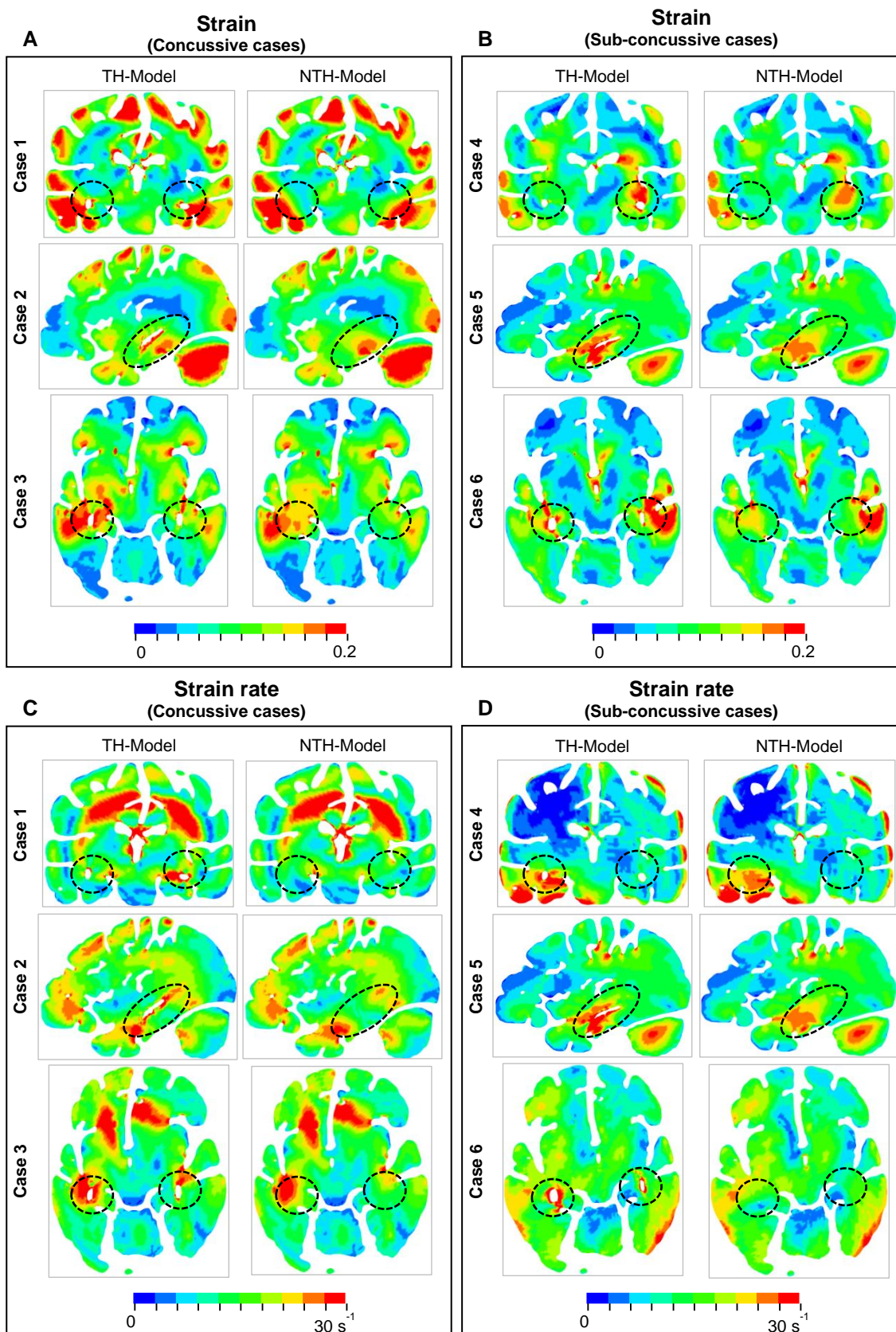
Fig. 3. Comparison of the maximum principal strain (A and B) and strain rate (C and D) distribution between the TH-model and NTH-model for three concussive and three sub-concussive impacts (Cases 1-3 and 4-6 respectively). The temporal horn and adjacent tissue are highlighted by black dashed ellipses.

15

347   Close-up views of hippocampal strain and strain rate contours are presented in Fig. 4. Based

348   on visual observation, regions experiencing strain over 0.2 in the TH-Model were more extensive

349   with respect to their counterparts in the NTH-Model (Fig. 4A-B). This is particularly evident in

350   CA1, CA2/3, and CA4/DG. Similarly, a more widespread distribution of strain rate over 30 s^{-1} was

351   predicted by the TH-Model than the NTH-Model (Fig. 4C-D) in CA1, CA2/3, and HP Tail. This

352   visual observation is quantitatively confirmed in Appendix D, in which larger volume ratios of

353   strain over 0.2 and strain rate over 30 s^{-1} in the hippocampal subfields and the whole hippocampal

354   level were predicted by the TH-Model with respect to the NTH-Model.
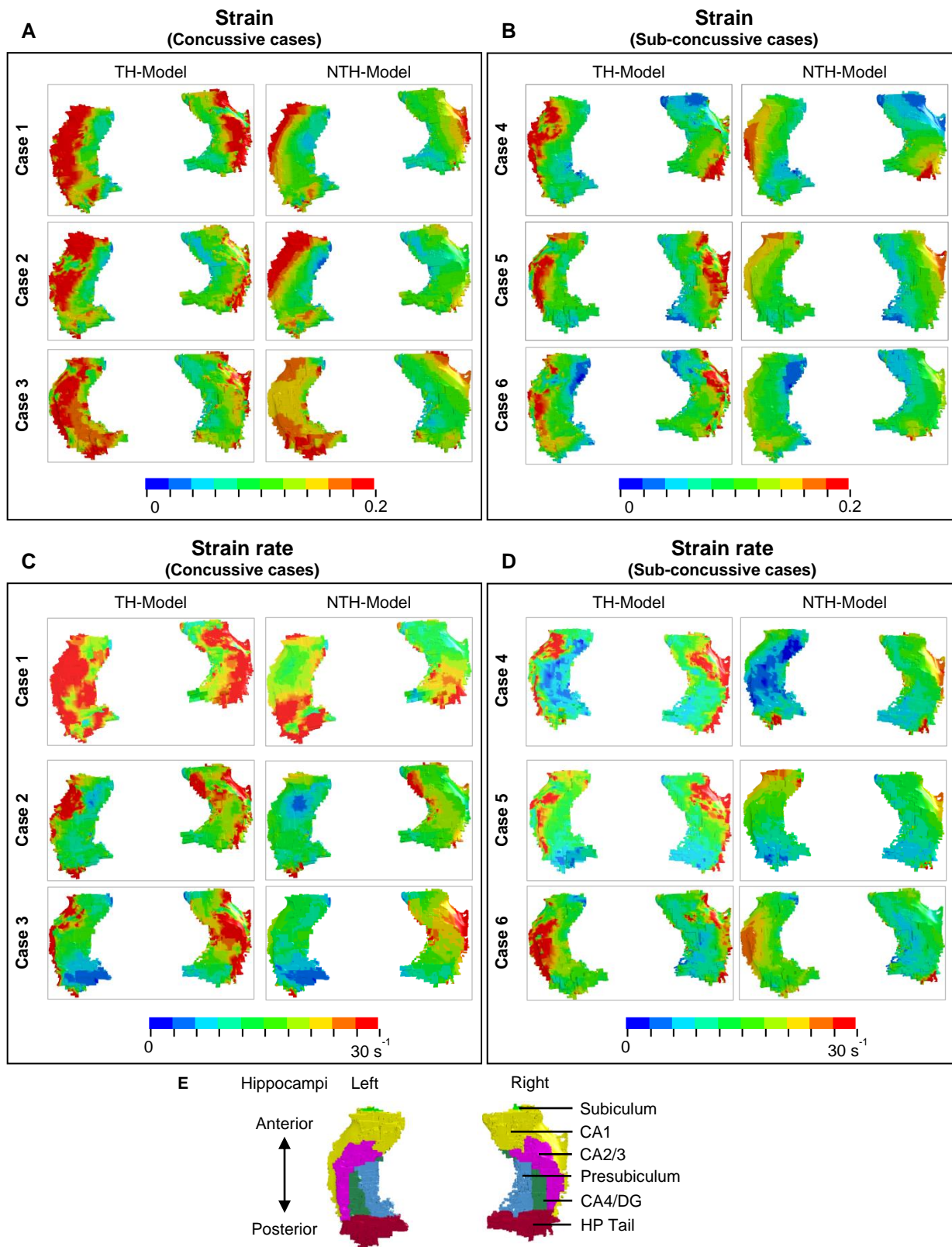
Fig. 4. Comparison of strain distribution (A and B) and strain rate distribution (C and D) in the hippocampi between the TH-model and NTH-model of three concussive impacts (Cases 1-3) and three sub-concussive impacts (Cases 4-6). Subfigure (**E**) illustrates the hippocampal subfields. CA: cornu ammonis; DG: dentate gyrus; HP Tail: hippocampal tail.

361   Fig 5 shows a quantitative depiction of the findings in Fig. 4 with special focus on the

362   peaking values: the addition of the temporal horn elevated the 95th percentile maximum principal

363   strain for almost all subfields and the whole hippocampus under all loading cases with the largest

364   elevation (111.0 %) noted in CA2/3 in Case 5 (Fig. 4A-B). Similarly, the 95th percentile maximum

365   strain rate was increased per the addition of the temporal horn for almost all hippocampal subfields

366   and the whole hippocampus, with the largest increase (168.0%) in HP Tail in Case 2 (Fig. 4C-D).

367   Any decrements in strain or strain rate were less than 5%.

Fig. 5. Comparison of the 95th percentile maximum principle strain and strain rate in the hippocampal subfields and the whole hippocampus between the TH-Model and NTH-model of 3 concussive impacts (Cases 1-3) and 3 sub-concussive impacts (Cases 4-6). (**A**) Comparison of strain in the hippocampal subfields of 3 concussive impacts. (**B**) Comparison of strain in the hippocampal subfields of 3 sub-concussive impacts. (**C**) Comparison of strain rate in the hippocampal subfields of 3 concussive impacts. (**D**) Comparison of strain rate in the hippocampal subfields of 3 sub-concussive impacts. Percentages in strain difference and strain rate difference

19

are calculated with the results of the NTH-Model as the baseline. CA: cornu ammonis; DG: dentate gyrus; HP Tail: hippocampal tail.

We next aimed at identifying the anatomical regions most affected by the presence of the temporal horn. Using a Wilcoxon matched-pairs signed-rank tests on the region-wise strain and strain rate, we found considerable increases in strain (median value of percent strain difference>5%) on all six hippocampal subfields and the whole hippocampus at significant levels ($p<0.05$) (Table 3.A). For the strain rate, considerable increases (median value of percent strain rate difference>5%) were noted in all subfields except for the presubiculum.

Table 3. Wilcoxon matched-pairs signed-rank test on the region-wise strain and strain rate in the hippocampal subfields and whole hippocampus (A) and non-hippocampal regions (B) (N=6). Percentages in strain difference and strain rate difference between the TH-Model and NTH-model were calculated across all simulations and presented in the form of median and two quartile values with Q1 as 25th percentile value and Q3 as 75th percentile value. Note that N equals to the number of impacts simulated by each model. CA: cornu ammonis; DG: dentate gyrus; HP Tail: hippocampal tail; Ventral DC: ventral diencephalon; CC: corpus callosum.

A	Regions	Percentage in strain difference (median (Q1, Q3)) (%)	p	Percentage in strain rate difference (median (Q1, Q3)) (%)	p
	CA1	44.6 (33.6, 53.0)	0.028	92.3 (69.3, 98.5)	0.028
	CA2/3	64.6 (62.7, 104.3)	0.028	97.9 (81.0, 121.0)	0.028
	CA4/DG	11.7 (3.2, 21.8)	0.046	23.7 (17.2, 67.6)	0.028
	HP Tail	33.9 (18.6, 54.3)	0.046	35.5 (12.5, 67.6)	0.046
	Subiculum	6.9 (5.5, 11.2)	0.046	65.3 (61.6, 89.7)	0.028
	Presubiculum	19.9 (11.6, 28.0)	0.028	2.7 (1.9, 3.7)	0.046
	Hippocampus	29.5 (25.3, 33.2)	0.028	57.5 (34.7, 91.9)	0.028
B	Regions	Percentage in strain difference (median (Q1, Q3)) (%)	p	Percentage in strain rate difference (median (Q1, Q3)) (%)	p
	Amygdala	33.8 (17.1, 39.3)	0.028	50.9 (40.4, 56.1)	0.028
	Ventral DC	8.2 (4.6, 12.2)	0.028	9.35 (3.7, 13.1)	0.028
	Pallidum	-1.7 (-4.2, 2.1)	0.249	-0.6 (-4.2, 4.4)	0.753
	Putamen	-1.4 (-2.3, 2.8)	0.249	2.2 (-0.4, 4.7)	0.173
	Caudate	1.5 (0.7, 5.5)	0.917	0.1 (-2.5, 0.9)	0.463
	CC	0.7 (0.0, 1.3)	0.249	2.5 (-0.4, 3.6)	0.116

Among the non-hippocampal regions, both strain and strain rate were elevated in the TH-Model in the amygdala, which is along the anterosuperior border of the temporal horn, and to a lesser extent in the nearby ventral DC (Appendix E, Table 3.B). For the remaining more-distant

394   regions, percentage differences in strain and strain rate were constantly less than 5% across the

395   simulated loading cases.

Stress in hippocampus and temporal horn

397   We then went on to explain the biomechanical reason for the hippocampal vulnerability. To

398   ascertain the alteration of stress transmission associated with the temporal horn, Fig. 6A-B

399   illustrates the maximum shear stress (i.e., a force triggering critical tissue deformation) endured by

400   the temporal horn and hippocampus in the TH-Model and their counterparts in the NTH-Model,

401   respectively. A much larger magnitude of shear stress in the hippocampus was noted in the TH-

402   Model compared to the NTH-Model across all the cases (Fig. 6A). Conversely, the maximum shear

403   stresses were less than 100 Pa in the temporal horn in the TH-Model, and over 1000 Pa in the

404   temporal horn substitute in the NTH-Model (Fig. 6B). In addition, the distribution of shear stress

405   within the hippocampus and temporal horn for one representative cases (Case 2) are illustrated in

406   Fig. 6C-D, in which a wider distribution of shear stress over 1000 Pa in the hippocampus was noted

407   in the TH-Model compared to the NTH-Model. It is thus indicated that an altered stress transmission

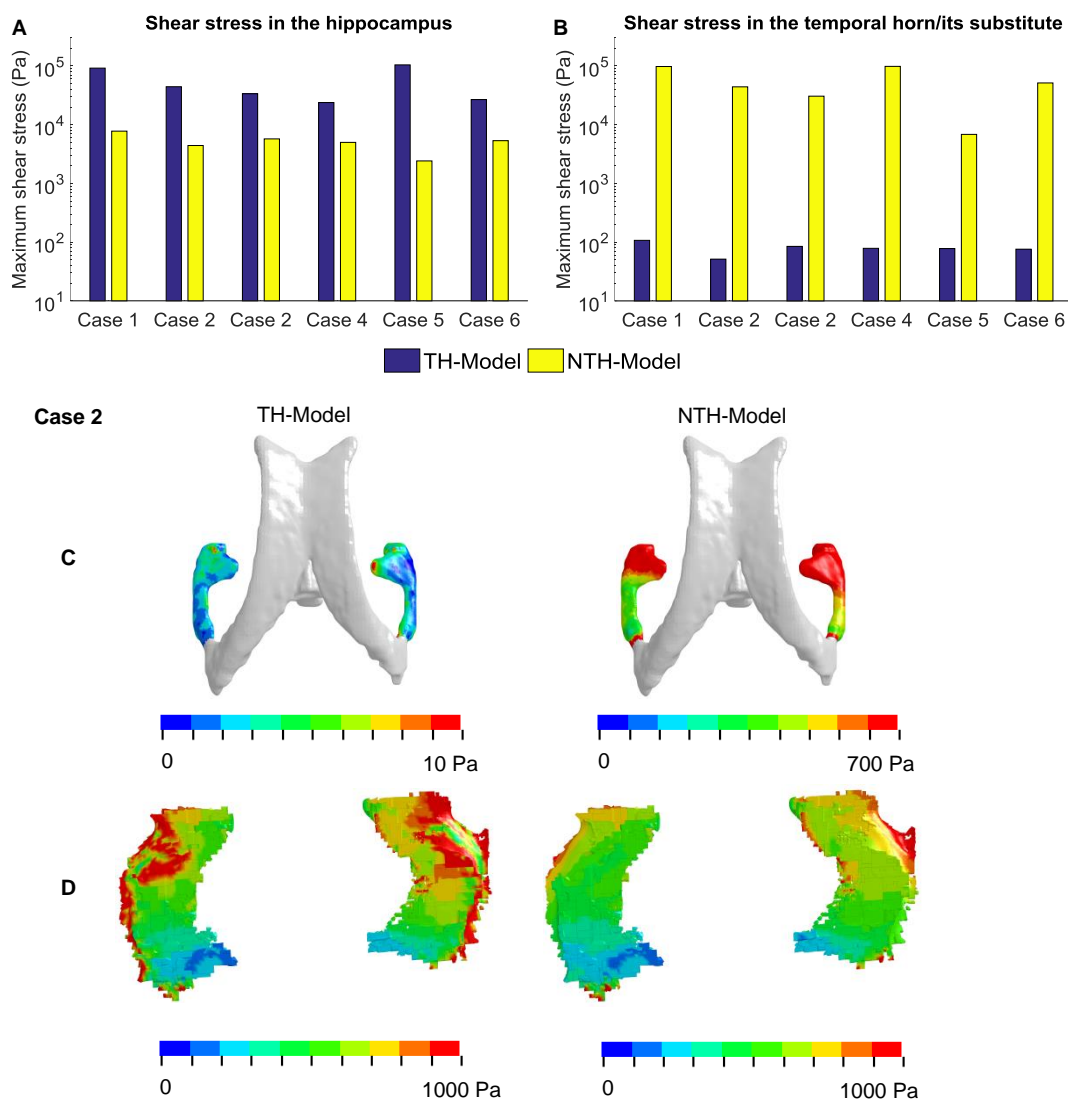408   associated with the temporal horn causes elevations in strain and strain rate.

Fig. 6. Maximum shear stresses in the hippocampus (A) and temporal horn/its substitute (B) predicted by the TH-Model and NTH-Model in 6 cases; (C) Contours of maximum shear stress in the CSF within the temporal horn in the TH-Model and its substitute in the NTH-Model; (D) Contours of maximum shear stress endured by the hippocampi in the TH-Model and NTH-Model. Note that, in the NTH-Model, the temporal horn is modeled as brain, not fluid.

Neuroimaging analysis

We then sought to identify if increased strains associated with the presence of the temporal horn would potentially be reflected in the volumetric relationship between the temporal horn and hippocampus in living subjects. We analyzed MRI of 91 male collegiate athletes (59 football (22 with a history of prior concussion), 32 volleyball (2 with a history of prior concussion), mean age (standard deviation) = 19.3 (1.43) years) to determine the volumetric relationship between the hippocampus and temporal horn by segmenting T1- and T2-weighted images, regressing out head size. The temporal horn size and total hippocampal volume were found to have a negative linear

22

423 relationship (coefficient [difference in hippocampal volume over difference in temporal horn

424 volume] = -0.929, p=0.001) (Fig. 7A). Inverse linear correlations between temporal horn volume

425 and subfield volumes were found in CA1 (coefficient = -0.294, p=0.002*(note that * represents a

426 threshold of 0.017 was attained for the survives multiple comparison correction)) (Fig. 7B), CA2-

427 4/DG (coefficient = -0.176, p=0.019) (Fig. 7C), and ERC/PRC (coefficient = -0.383, p=0.027), but

428 not in the subiculum (coefficient = -0.072, p=0.056).. After excluding the two outliers with the

429 temporal horn volume over 1000 mm^3, correlations of temporal horn with total hippocampal

430 volume (coefficient = -0.892, p=0.030), CA1 (coefficient = -0.288, p=0.037), and CA2-4/DG

431 (coefficient = -0.222, p=0.039) remained significant, while the correlation with ERC/PRC volume

432 was no longer significant (p=0.180).
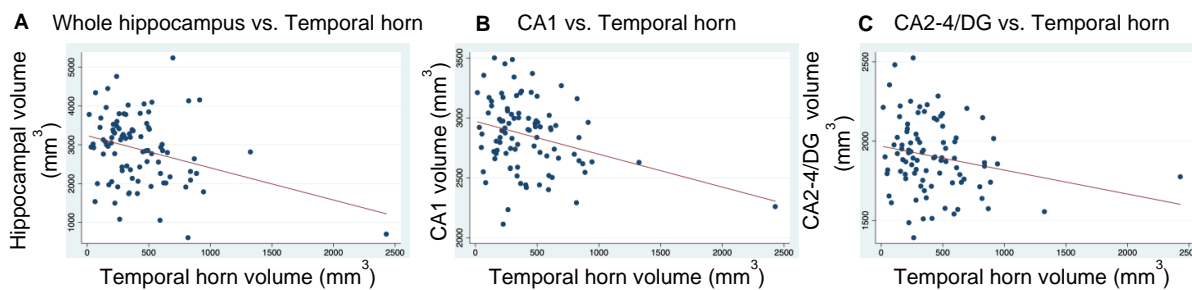
433

434 **Fig. 7. Inverse volumetric relationship of temporal horn with the whole hippocampus (A),**
435 **with CA1 (B), and with CA2-4/DG (C), derived using automated segmentation using ASHS**
436 **of *in vivo* data on 91 participants.**

437 # Discussion

438 The current study attempted to elucidate why the hippocampus is so commonly affected by

439 brain trauma. We used two FE models: one with and the other without the temporal horn, and

440 incorporated an anatomically accurate description of temporal horn, a mechanically realistic

441 representation of intraventricular CSF as fluid elements, and a fluid-structure interaction coupling

442 approach for the brain-ventricle interface. The presence of the temporal horn not only extended the

443 distribution of high strains and strain rates in the surrounding area, but also increased their

444 magnitude in the hippocampus, particularly in the subfields of CA1, CA2/3, HP Tail, subiculum,

445 and presubiculum. Other adjacent regions including the amygdala and ventral DC showed similarly

23

446 increased strain and strain rate with the presence of the temporal horn, but distant regions (e.g.,

447 corpus callosum) did not. These computational findings support the hypothesis that the presence of

448 the temporal horn exacerbates the biomechanical vulnerability of the hippocampus following head

449 impacts, yielding a potential biomechanical explanation for the prevalence of hippocampal injury

450 in TBI. In addition, our *in* vivo neuroimaging analysis in a collegiate athlete cohort revealed that

451 the volume of the temporal horn is inversely correlated with the hippocampal volume.

452   This biomechanical finding correlates well with the prevalence of hippocampal trauma in

453 humans data and animal biomechanical models. Several postmortem neuropathological studies

454 (Kotapka et al., 1992;Kotapka et al., 1993;Kotapka et al., 1994;Maxwell et al., 2003) have detected

455 overt neuronal damage/loss in the hippocampus of TBI victims with high incidence rates up to 73%-

456 87% (although the exact loadings endured were lacking). Animal models employing custom-built

457 pneumatic devices that deliver impulsive angular accelerations, similar to the loading mode in the

458 current study, have shown hippocampal lesions in non-human primates (Gennarelli et al.,

459 1982;Kotapka et al., 1991), which have a similar hippocampal morphology and spatial relationship

460 to the temporal horn (Insausti and Amaral, 2003;Amaral et al., 2007). A version of the device

461 modified to deliver impulsive loading caused selective hippocampal damage to porcine brains

462 (Smith et al., 1997) (which again have a similar relationship between the hippocampus and temporal

463 horn to humans (Félix et al., 1999)). Thus, animal models with similar morphological relationships

464 between the temporal horn and hippocampus support a biomechanical link between the two.

465   Our computational results predicted an altered stress transmission associated with the

466 temporal horn, providing an explanation for the elevations in strain and strain rate in the TH-Model.

467 As illustrated in Fig. 6B, the shear stress endured by the temporal horn in the TH-Model was less

468 than 100 Pa, which realistically reflected the low shear resistance nature of CSF. Comparatively,

469 the shear stress experienced by the substitute of the temporal horn (i.e., brain parenchyma) in the

470 NTH-Model was over 1000 Pa, providing an unrealistic interaction with the neighboring tissue.

24

471 These regions adjacent to the temporal horn (such as the hippocampus, amygdala, and ventral DC,

472 as are the ROIs in the current study) were easier to deform associated with the addition of the

473 temporal horn in the TH-Model, consequently exacerbating the strain and strain rate in these ROIs.

474 This explanation was further verified in Fig. 6A, where the shear stress endured by the hippocampus

475 was larger in the TH-Model, consistent with an amplified force exerted on the hippocampus with

476 the addition of the temporal horn.

477 Two previous computational studies simulated football head impacts, consistently reporting

478 an increased susceptibility of the hippocampus to injury (Viano et al., 2005;Zhao et al., 2017).

479 However, the ventricular elements in these two models and other ones (Kleiven, 2007;Mao et al.,

480 2013;Atsumi et al., 2018;Trotta et al., 2020) were manually picked with reference to the brain atlas,

481 lacking mesh conformity of the anatomic ventricle profile. Our work used a novel FE model of the

482 brain that involves orders of magnitude more elements than used in typical models (e.g., millions

483 instead of thousands), enabling a realistic depiction of the geometrical features of the temporal horn.

484 Intraventricular CSF elements in existing head models (Viano et al., 2005;Kimpara et al.,

485 2006;Takhounts et al., 2008;Mao et al., 2013;Ho et al., 2017;Zhao et al., 2017;Zhou et al., 2019a;Li

486 et al., 2020) are predominantly represented by Lagrangian elements, with the mesh following the

487 material deformation without material advection, neglecting the potential fluid flow during the

488 impact. Here, we leveraged a fluid element formulation (i.e., ALE multi-material formulation) for

489 the cerebral ventricle, emulating the fluid properties of intraventricular CSF and potential fluid flow

490 following external stimuli. To couple the mechanical responses of the ALE-represented ventricular

491 CSF elements with the Lagrangian-represented brain elements, a penalty-based coupling was

492 implemented. Such a coupling algorithm permits relative motion in the tangential direction and

493 deliveries tension and compression in the radial direction, circumventing severe element distortion

494 at the interfacial boundary. The FSI approach excels in not only realistically representing the fluid

495 behavior of the CSF but also maintaining numerical stability without causing severe element

496   distortion, supporting its validity for the current application. Nevertheless, it is worth clarifying that

497   our data suggest that omitting the temporal horn, as is the case in most existing head models, may

498   still be acceptable for these studies that focus on regions far from the temporal horn (e.g., corpus

499   callosum, caudate, putamen, pallidum).

500   Hippocampal cell death tolerance criteria were presented by Cater et al. (2006) by relating

501   three independent variables (i.e., strain in the range of 0.05 to 0.5, hippocampal subfields, time

502   post-injury) to resultant cell death under *in vitro* conditions via mathematical equations, which were

503   valid within the strain rate regime of 0.1-50 s^{-1}. Similarly, another *in vitro* study reported tolerance

504   criteria for hippocampal function impairment in the form of mathematical formulations between

505   input mechanical stimuli (i.e., strain up to 0.44 and strain rate up to 30 s^{-1}) and output

506   electrophysiological alterations (Kang and Morrison, 2015). In the current study, the hippocampal

507   responses predicted by the TH-Model peaking from 0.29 to 0.50 for strain and from 53.9 s^{-1} to 93.6

508   s^{-1} for strain rate in the six simulated impacts. The range of FE-derived strains and strain rates

509   reached the criteria of electrophysiological impairment and cell death, correlating with the clinical

510   diagnosis of concussion and sub-concussion of the players. However, it should be noted that certain

511   disparities existed between the data ranges of the current computational results and the loading

512   regimes from which these two hippocampus-related tolerance criteria were fitted. Moreover, the

513   cultured hippocampal slices in Cater et al. (2006) and Kang and Morrison (2015) were obtained

514   from the rat brain. Extrapolation of the tolerance criteria derived from the animal brain under *in*

515   *vitro* conditions to the human brain under *in vivo* conditions requires further verification (Seok et

516   al., 2013).

517   While the presence of the CSF-filled temporal horn may be a predisposing factor for

518   hippocampal injury, additional mechanisms, such as the selective vulnerability of hippocampal

519   neurons to hypoxemia and ischemia (Pulsinelli, 1985;Ng et al., 1989) and pathological neuronal

520   excitation involving glutamate and other excitatory amino acid neurotransmitters (Faden et al.,

26

521 1989;Bullock et al., 1990), may play important roles in human hippocampal injury. We suggest that

522 the adverse effects of the temporal horn during the primary impact, the superimposed

523 hypoxia/ischemia and neuroexcitotoxicity secondary to the impact, as well as other potential

524 unknown mechanisms, collectively contribute to the prevalence of hippocampal injury in TBI

525 victims.

526 To see if the modeled relationship between the presence of the temporal horn and associated

527 increased strains/strain rates had an *in vivo* correlation, we analyzed the neuroimaging of 91

528 participants without a prior history of severe brain injury (though several did have a concussion

529 history). The temporal horn size was inversely correlated with both the total hippocampus volume

530 and several hippocampal subfields, including CA1 and CA2-4/DG, in this collegiate cohort. The

531 lower hippocampal volume might possibly be secondary to injury from the increased strain/strain

532 rate associated with the presence of the temporal horn. This finding reflects prior work in TBI

533 (Bigler et al., 1997), in which a negative correlation between temporal horn size and hippocampal

534 volume was only noted within the cohort of TBI patients, not in the control group. Such a disparity

535 might be associated with the aging difference of enrolled subjects between our work and the

536 previous study. In our work, the enrolled subjects were male collegiate students (mean age ±

537 standard deviation: 19.3 ± 1.43 years). The age of controlled subjects in the previous study (Bigler

538 et al., 1997) ranged from 16-year-old to 65-year-old. Such a wide age window may further

539 compound the relationship of the hippocampus and temporal horn considering the development

540 variation to the brain in normal aging (Van Petten, 2004). However, it should be clarified that the

541 exact source responsible for this disparity remains elusive.

542 **Limitations and future work**

543 Although the current study yielded some new insights into the biomechanical and

544 volumetric dependencies of the hippocampus on the temporal horn, certain limitations exist which

545 require further investigation. First, only 6 representative sports-related inertial impacts were

27

546 simulated in the current study with the severities at concussive and sub-concussive levels. A

547 systematic investigation that covers more impact-related variables (e.g., impact duration, impact

548 directions, rotational velocity) with their magnitudes spanning over the regimes measured from the

549 realistic impacts is planned for future work to identify the critical scenarios that the temporal horn

550 exhibited a more pronounced effect on the hippocampus. Moreover, caution should be exercised

551 when extrapolating the current findings obtained from concussive and sub-concussive impacts to

552 extra injury scenarios (e.g., fatal brain injury, penetrating head injury).

553 Secondly, due to the computational challenges, the brain-skull interfaces in both models in

554 the current study were simulated by approximating the subarachnoid CSF as a Lagrangian-

555 represented structure. Given that the ROIs in the current study are all located at central brain regions,

556 the influence exerted by the brain-skull influence on the deep brain structures was expected to be

557 limited (Kleiven and Hardy, 2002). Per the benefits of using ALE elements for the cerebral

558 ventricles, the impact-induced fluid flow was considered, but not quantified in the current study. A

559 detailed examination of flow patterns of CSF remains to be appropriately quantified in the future

560 (Lang and Wu, 2021).

561 Thirdly, to incorporate explicit representations of the hippocampal subfields in the FE

562 models, Freesurfer was used to segment the MRI with a resolution of $1 \times 1 \times 1$ mm^3 to take

563 advantage of the isotropic high-resolution atlas and incorporate this detailed isotropic segmentation

564 into the FE model. Such a software choice was also for the consistency purpose, since the brain

565 profile used for the development of FE model was obtained from Freesurfer. However, it should be

566 highlighted there are many different segmentation methods for hippocampal subfields, presenting

567 certain variances in specific subfield delineation (Yushkevich et al., 2015;Wisse et al., 2021). Thus,

568 caution should be exercised when using Freesurfer for hippocampal subfield segmentation (Wisse

569 et al., 2014). In fact, there appear no approaches with guaranteed utility and validity to segment

570 hippocampal subfield from isotropic 1 mm^3 MRI (Wisse et al., 2021), as is the case for the subfield

28

571 delineation in the FE model. This segment-induced error inevitably compromised the accuracy of

572 hippocampal subfield representations in the FE model, which is a limitation of the current study.

573 Nevertheless, compared with the studies in which the hippocampus was treated as a single medium

574 (Takhounts et al., 2008;Mao et al., 2013;Miller et al., 2016;Atsumi et al., 2018;Li et al., 2020;Trotta

575 et al., 2020;Zhou et al., 2020a), the current work made the first step to differentiate the hippocampal

576 substructures in the FE model of the human brain. Future work is planned to further refine the

577 model towards an anatomically more authentic hippocampal subfield representation. For the in vivo

578 imaging, we sought to determine individual subject differences, and have a fully characterized and

579 quality-control assessed segmentation on high-resolution anisotropic data using ASHS in this large

580 cohort. While the differences in these two segmentation methods used in the current work, they

581 both show differences in the central hippocampus (CA3/4/DG), which is not a high region of

582 variability between segmentation methods (Yushkevich et al., 2015).

583 Lastly, the subjects involved in the neuroimaging analysis were not those with the impacts

584 simulated using the computational models. Thus, it remains to be further verified whether the lower

585 hippocampal volume observed from the collegiate athletes is due to the increased strain/strain rate

586 associated with the presence of the temporal horn during head impacts versus other factors.

587 Ongoing effort is dedicated to deploy instrumented mouthguards to football players, obtaining real-

588 time measurements of the impacts sustained by these players (Camarillo et al., 2013;Hernandez et

589 al., 2015;Domel et al., 2020;Liu et al., 2020b). This information is complemented by medical

590 imaging of the football players pre- and post-impact (Parivash et al., 2019;Mills et al., 2020).

591 Another possible direction for future work is to correlate on-field football impacts, to

592 computationally predicted hippocampal deformation, to image-based evidence of hippocampal

593 injury.

594 ## Conclusion

595   This study investigated the biomechanical mechanism of hippocampal injury associated

596 with the presence of the temporal horn by leveraging two models, with and without the inclusion

597 of the temporal horn. The results showed that the temporal horn has a significant biomechanical

598 effect in the surrounding area and induces increased magnitudes of the strain and strain rate in the

599 hippocampus throughout its subfields, identifying the temporal horn as a predisposing factor for

600 hippocampal injury. Our *in vivo* human imaging analysis revealed that the volume of the temporal

601 horn is inversely correlated with the hippocampal volume and hippocampal subfields commonly

602 involved in hippocampal injury. Our biomechanical and neuroimaging effort collectively highlight

603 the mechanobiological and anatomical interdependency between the hippocampus and temporal

604 horn. This study suggests that proper modeling of the temporal horn be considered when developing

605 mechanical tolerance and designing protective strategies specifically for the hippocampus.

Acknowledgements

References

Aimedieu, P., and Grebe, R. (2004). Tensile strength of cranial pia mater: preliminary results. *Journal of neurosurgery* 100**,** 111-114.

Amaral, D., Andersen, P., O'keefe, J., and Morris, R. (2007). *The hippocampus book.* Oxford University Press.

Anderson, R.W., Brown, C.J., Blumbergs, P.C., Mclean, A.J., and Jones, N.R. (2003). Impact mechanics and axonal injury in a sheep model. *Journal of neurotrauma* 20**,** 961-974.

Atsumi, N., Nakahira, Y., Tanaka, E., and Iwamoto, M. (2018). Human brain modeling with its anatomical structure and realistic material properties for brain injury prediction. *Annals of biomedical engineering* 46**,** 736-748.

Baldwin, S.A., Gibson, T., Callihan, C.T., Sullivan, P.G., Palmer, E., and Scheff, S.W. (1997). Neuronal cell loss in the CA3 subfield of the hippocampus following cortical contusion utilizing the optical disector method for cell counting. *Journal of neurotrauma* 14**,** 385-398.

Barnes, J., Ridgway, G.R., Bartlett, J., Henley, S.M., Lehmann, M., Hobbs, N., Clarkson, M.J., Macmanus, D.G., Ourselin, S., and Fox, N.C. (2010). Head size, age and gender adjustment in MRI studies: a necessary nuisance? *Neuroimage* 53**,** 1244-1255.

Batterbee, D., Sims, N., Becker, W., Worden, K., and Rowson, J. (2011). Computational model of an infant brain subjected to periodic motion simplified modelling and bayesian sensitivity analysis. *Proceedings of the Institution of Mechanical Engineers, Part H: Journal of Engineering in Medicine* 225**,** 1036-1049.

Bigler, E.D., Andersob, C.V., and Blatter, D.D. (2002). Temporal lobe morphology in normal aging and traumatic brain injury. *American Journal of Neuroradiology* 23**,** 255-266.

Bigler, E.D., Blatter, D.D., Anderson, C.V., Johnson, S.C., Gale, S.D., Hopkins, R.O., and Burnett, B. (1997). Hippocampal volume in normal aging and traumatic brain injury. *American Journal of Neuroradiology* 18**,** 11-23.

Bigler, E.D., and Tate, D.F. (2001). Brain volume, intracranial volume, and dementia. *Investigative radiology* 36**,** 539-546.

Bird, C.M., and Burgess, N. (2008). The hippocampus and memory: insights from spatial processing. *Nature Reviews Neuroscience* 9**,** 182-194.

Bullock, R., Butcher, S., and Mcculloch, J. (1990). "Changes in extracellular glutamate concentration after acute subdural haematoma in the rat—evidence for an "excitotoxic" mechanism?," in *Brain Edema VIII*. Springer), 274-276.

Camarillo, D.B., Shull, P.B., Mattson, J., Shultz, R., and Garza, D. (2013). An instrumented mouthguard for measuring linear and angular head impact kinematics in American football. *Annals of biomedical engineering* 41**,** 1939-1949.

Cameron, K.L., Marshall, S.W., Sturdivant, R.X., and Lincoln, A.E. (2012). Trends in the incidence of physician-diagnosed mild traumatic brain injury among active duty US military personnel between 1997 and 2007. *Journal of neurotrauma* 29**,** 1313-1321.

Cater, H.L., Sundstrom, L.E., and Morrison Iii, B. (2006). Temporal development of hippocampal cell death is dependent on tissue strain but not strain rate. *Journal of biomechanics* 39**,** 2810-2818.

Cecchi, N.J., Domel, A.G., Liu, Y., Rice, E., Lu, R., Zhan, X., Zhou, Z., Raymond, S.J., Sami, S., and Singh, H. (2021). Identifying Factors Associated with Head Impact Kinematics and Brain Strain in High School American Football via Instrumented Mouthguards. *Annals of Biomedical Engineering***,** 1-13.

Contijoch, F., Witschey, W.R., Rogers, K., Rears, H., Hansen, M., Yushkevich, P., Gorman, J., Gorman, R.C., and Han, Y. (2015). User-initialized active contour segmentation and golden-angle real-time cardiovascular magnetic resonance enable accurate assessment of

669   LV function in patients with sinus rhythm and arrhythmias. *Journal of cardiovascular*
670   *magnetic resonance* 17**,** 1-12.

671 Dewan, M.C., Rattani, A., Gupta, S., Baticulon, R.E., Hung, Y.-C., Punchak, M., Agrawal, A.,
672   Adeleye, A.O., Shrime, M.G., and Rubiano, A.M. (2018). Estimating the global incidence
673   of traumatic brain injury. *Journal of neurosurgery* 130**,** 1080-1097.

674 Domel, A.G., Raymond, S.J., Giordano, C., Liu, Y., Yousefsani, S.A., Fanton, M., Pirozzi, I.,
675   Kight, A., Avery, B., Boumis, A., Fetters, T., Jandu, S., Mehring, W.M., Monga, S.,
676   Mouchawar, N., Rangel, I., Rice, E., Roy, P., Sami, S., Singh, H., Wu, L., Kuo, C.,
677   Zeineh, M., Grant, G., and Camarillo, D.B. (2020). A New Open-Access Platform for
678   Measuring and Sharing mTBI Data. *arXiv:2010.08485*.

679 Faden, A.I., Demediuk, P., Panter, S.S., and Vink, R. (1989). The role of excitatory amino acids
680   and NMDA receptors in traumatic brain injury. *Science* 244**,** 798-800.

681 Félix, B., Léger, M.-E., Albe-Fessard, D., Marcilloux, J.-C., Rampin, O., Laplace, J.-P., Duclos,
682   A., Fort, F., Gougis, S., and Costa, M. (1999). Stereotaxic atlas of the pig brain. *Brain*
683   *research bulletin* 49**,** 1-137.

684 Fillmore, P.T., Phillips-Meek, M.C., and Richards, J.E. (2015). Age-specific MRI brain and head
685   templates for healthy adults from 20 through 89 years of age. *Frontiers in aging*
686   *neuroscience* 7**,** 44.

687 Fischl, B. (2012). FreeSurfer. *Neuroimage* 62**,** 774-781.

688 Gale, S.D., Johnson, S.C., Bigler, E.D., and Blatter, D.D. (1994). Traumatic brain injury and
689   temporal horn enlargement: Correlates with tests of intelligence and memory.
690   *Neuropsychiatry, Neuropsychology, & Behavioral Neurology* 7**,** 160-165.

691 Gennarelli, T.A., Thibault, L.E., Adams, J.H., Graham, D.I., Thompson, C.J., and Marcincin, R.P.
692   (1982). Diffuse axonal injury and traumatic coma in the primate. *Annals of Neurology:*
693   *Official Journal of the American Neurological Association and the Child Neurology*
694   *Society* 12**,** 564-574.

695 Graham, D., Adams, J.H., and Doyle, D. (1978). Ischaemic brain damage in fatal non-missile
696   head injuries. *Journal of the neurological sciences* 39**,** 213-234.

697 Graham, D., Ford, I., Adams, J.H., Doyle, D., Teasdale, G., Lawrence, A., and Mclellan, D.
698   (1989). Ischaemic brain damage is still common in fatal non-missile head injury. *Journal*
699   *of Neurology, Neurosurgery & Psychiatry* 52**,** 346-350.

700 Hallquist, J.O. (2007). "LS-DYNA keyword user's manual", in: *Livermore Software Technology*
701   *Corporation.*).

702 Hardy, W.N., Mason, M.J., Foster, C.D., Shah, C.S., Kopacz, J.M., Yang, K.H., King, A.I.,
703   Bishop, J., Bey, M., and Anderst, W. (2007). A Study of the Response of the Human
704   Cadaver Head to Impact. *Stapp Car Crash J* 51**,** 17-80.

705 Hernandez, F., Wu, L.C., Yip, M.C., Laksari, K., Hoffman, A.R., Lopez, J.R., Grant, G.A.,
706   Kleiven, S., and Camarillo, D.B. (2015). Six degree-of-freedom measurements of human
707   mild traumatic brain injury. *Annals of biomedical engineering* 43**,** 1918-1934.

708 Hicks, R., Soares, H., Smith, D., and Mcintosh, T. (1996). Temporal and spatial characterization
709   of neuronal injury following lateral fluid-percussion brain injury in the rat. *Acta*
710   *neuropathologica* 91**,** 236-246.

711 Ho, J., Zhou, Z., Li, X., and Kleiven, S. (2017). The peculiar properties of the falx and tentorium
712   in brain injury biomechanics. *Journal of biomechanics* 60**,** 243-247.

713 Holzapfel, A.G. (2000). Nonlinear solid mechanics II.

714 Insausti, R., and Amaral, D.G. (2003). "Hippocampal formation," in *The Human Nervous System:*
715   *Second Edition*. Elsevier Inc.), 871-914.

716 Ji, S., Zhao, W., Ford, J.C., Beckwith, J.G., Bolander, R.P., Greenwald, R.M., Flashman, L.A.,
717   Paulsen, K.D., and Mcallister, T.W. (2015). Group-wise evaluation and comparison of

white matter fiber strain and maximum principal strain in sports-related concussion. *Journal of neurotrauma* 32, 441-454.

Kalish, B.T., and Whalen, M.J. (2016). "Weight drop models in traumatic brain injury," in *Injury models of the central nervous system*. Springer), 193-209.

Kang, W.H., and Morrison, B. (2015). Functional tolerance to mechanical deformation developed from organotypic hippocampal slice cultures. *Biomechanics and Modeling in Mechanobiology* 14, 561-575.

Kimpara, H., Nakahira, Y., Iwamoto, M., and Miki, K. (2006). Investigation of Anteroposterior Head-Neck Responses during Severe Frontal Impacts Using a Brain-Spinal Cord Complex FE Model. *Stapp Car Crash Journal* 50, 509-544.

Kleiven, S. (2007). Predictors for traumatic brain injuries evaluated through accident reconstructions. *Stapp car crash journal* 51, 81-114.

Kleiven, S., and Hardy, W.N. (2002). Correlation of an FE model of the human head with local brain motion-consequences for injury prediction. *Stapp Car Crash Journal* 46, 123-144.

Kotapka, M., Graham, D., Adams, J., and Gennarelli, T. (1992). Hippocampal pathology in fatal non-missile human head injury. *Acta neuropathologica* 83, 530-534.

Kotapka, M., Graham, D., Adams, J., and Gennarelli, T. (1994). Hippocampal pathology in fatal human head injury without high intracranial pressure. *Journal of neurotrauma* 11, 317-324.

Kotapka, M., Graham, D., Adams, J.H., Doyle, D., and Gennarelli, T. (1993). Hippocampal damage in fatal paediatric head injury. *Neuropathology and applied neurobiology* 19, 128-133.

Kotapka, M.J., Gennarelli, T.A., Graham, D.I., Adams, J.H., Thibault, L.E., Ross, D.T., and Ford, I. (1991). Selective vulnerability of hippocampal neurons in acceleration-induced experimental head injury. *Journal of neurotrauma* 8, 247-258.

Lang, J., and Wu, Q. (2021). Modelling of the transient cerebrospinal fluid flow under external impacts. *European Journal of Mechanics-B/Fluids*.

Langlois, J.A., and Sattin, R.W. (2005). Traumatic brain injury in the United States: Research and programs of the Centers for Disease Control and Prevention (CDC)-Preface. *Journal of Head Trauma Rehabilitation* 20, 187-188.

Leranth, C., Szeidemann, Z., Hsu, M., and Buzsaki, G. (1996). AMPA receptors in the rat and primate hippocampus: a possible absence of GluR2/3 subunits in most interneurons. *Neuroscience* 70, 631-652.

Li, J., and Ji, L. (2005). Adjusting multiple testing in multilocus analyses using the eigenvalues of a correlation matrix. *Heredity* 95, 221-227.

Li, X., Zhou, Z., and Kleiven, S. (2020). An anatomically detailed and personalizable head injury model: Significance of brain and white matter tract morphological variability on strain. *Biomechanics and Modeling in Mechanobiology*.

Liu, Y., Domel, A.G., Yousefsani, S.A., Kondic, J., Grant, G., Zeineh, M., and Camarillo, D.B. (2020a). Validation and comparison of instrumented mouthguards for measuring head kinematics and assessing brain deformation in football impacts. *Annals of Biomedical Engineering* 48, 2580-2598.

Liu, Y., Domel, A.G., Yousefsani, S.A., Kondic, J., Grant, G., Zeineh, M., and Camarillo, D.B. (2020b). Validation and Comparison of Instrumented Mouthguards for Measuring Head Kinematics and Assessing Brain Deformation in Football Impacts. *Annals of Biomedical Engineering*, 1-19.

Maas, A.I., Menon, D.K., Adelson, P.D., Andelic, N., Bell, M.J., Belli, A., Bragge, P., Brazinova, A., Büki, A., and Chesnut, R.M. (2017). Traumatic brain injury: integrated approaches to improve prevention, clinical care, and research. *The Lancet Neurology* 16, 987-1048.

Mao, H., Zhang, L., Jiang, B., Genthikatti, V.V., Jin, X., Zhu, F., Makwana, R., Gill, A., Jandir, G., and Singh, A. (2013). Development of a finite element human head model partially validated with thirty five experimental cases. *Journal of biomechanical engineering* 135.

Maréchal, L. (2009). "Advances in octree-based all-hexahedral mesh generation: handling sharp features," in *Proceedings of the 18th international meshing roundtable*. Springer), 65-84.

Maxwell, W., Dhillon, K., Harper, L., Espin, J., Macintosh, T., Smith, D., and Graham, D. (2003). There is differential loss of pyramidal cells from the human hippocampus with survival after blunt head injury. *Journal of Neuropathology & Experimental Neurology* 62**,** 272-279.

Mcallister, T.W., Ford, J.C., Ji, S., Beckwith, J.G., Flashman, L.A., Paulsen, K., and Greenwald, R.M. (2012). Maximum principal strain and strain rate associated with concussion diagnosis correlates with changes in corpus callosum white matter indices. *Annals of biomedical engineering* 40**,** 127-140.

Mckee, A.C., Stein, T.D., Kiernan, P.T., and Alvarez, V.E. (2015). The neuropathology of chronic traumatic encephalopathy. *Brain pathology* 25**,** 350-364.

Meier, T.B., Brummel, B.J., Singh, R., Nerio, C.J., Polanski, D.W., and Bellgowan, P.S. (2015). The underreporting of self-reported symptoms following sports-related concussion. *Journal of science and medicine in sport* 18**,** 507-511.

Miller, L.E., Urban, J.E., and Stitzel, J.D. (2016). Development and validation of an atlas-based finite element brain model. *Biomechanics and modeling in mechanobiology* 15**,** 1201-1214.

Mills, B.D., Goubran, M., Parivash, S.N., Dennis, E.L., Rezaii, P., Akers, C., Bian, W., Mitchell, L.A., Boldt, B., and Douglas, D. (2020). Longitudinal alteration of cortical thickness and volume in high-impact sports. *NeuroImage***,** 116864.

Ng, T., Graham, D., Adams, J., and Ford, I. (1989). Changes in the hippocampus and the cerebellum resulting from hypoxic insults: frequency and distribution. *Acta neuropathologica* 78**,** 438-443.

Panzer, M.B., Myers, B.S., Capehart, B.P., and Bass, C.R. (2012). Development of a finite element model for blast brain injury and the effects of CSF cavitation. *Annals of biomedical engineering* 40**,** 1530-1544.

Parivash, S.N., Goubran, M., Mills, B.D., Rezaii, P., Thaler, C., Wolman, D., Bian, W., Mitchell, L.A., Boldt, B., and Douglas, D. (2019). Longitudinal changes in hippocampal subfield volume associated with collegiate football. *Journal of neurotrauma* 36**,** 2762-2773.

Parsons, C., Danysz, W., and Quack, G. (1999). Memantine is a clinically well tolerated N-methyl-D-aspartate (NMDA) receptor antagonist—a review of preclinical data. *Neuropharmacology* 38**,** 735-767.

Pellman, E.J., Viano, D.C., Tucker, A.M., Casson, I.R., and Waeckerle, J.F. (2003). Concussion in professional football: reconstruction of game impacts and injuries. *Neurosurgery* 53**,** 799-814.

Pieper, S., Halle, M., and Kikinis, R. (Year). "3D Slicer", in: *2004 2nd IEEE international symposium on biomedical imaging: nano to macro (IEEE Cat No. 04EX821)*: IEEE), 632-635.

Pulsinelli, W.A. (1985). "Selective neuronal vulnerability: morphological and molecular characteristics," in *Progress in brain research*. Elsevier), 29-37.

Roozenbeek, B., Maas, A.I., and Menon, D.K. (2013). Changing patterns in the epidemiology of traumatic brain injury. *Nature Reviews Neurology* 9**,** 231-236.

Rosenthal, J.A., Foraker, R.E., Collins, C.L., and Comstock, R.D. (2014). National high school athlete concussion rates from 2005-2006 to 2011-2012. *The American journal of sports medicine* 42**,** 1710-1715.

Runnerstam, M., Bao, F., Huang, Y., Shi, J., Gutierrez, E., Hamberger, A., Hansson, H.-A., Viano, D., and Haglid, K. (2001). A new model for diffuse brain injury by rotational acceleration: II. Effects on extracellular glutamate, intracranial pressure, and neuronal apoptosis. *Journal of neurotrauma* 18**,** 259-273.

Sanchez, E.J., Gabler, L.F., Good, A.B., Funk, J.R., Crandall, J.R., and Panzer, M.B. (2019). A reanalysis of football impact reconstructions for head kinematics and finite element modeling. *Clinical biomechanics* 64**,** 82-89.

Seok, J., Warren, H.S., Cuenca, A.G., Mindrinos, M.N., Baker, H.V., Xu, W., Richards, D.R., Mcdonald-Smith, G.P., Gao, H., and Hennessy, L. (2013). Genomic responses in mouse models poorly mimic human inflammatory diseases. *Proceedings of the National Academy of Sciences* 110**,** 3507-3512.

Singh, R., Meier, T.B., Kuplicki, R., Savitz, J., Mukai, I., Cavanagh, L., Allen, T., Teague, T.K., Nerio, C., and Polanski, D. (2014). Relationship of collegiate football experience and concussion with hippocampal volume and cognitive outcomes. *Jama* 311**,** 1883-1888.

Smith, D.H., Chen, X.-H., Xu, B.-N., Mcintosh, T.K., Gennarelli, T.A., and Meaney, D.E. (1997). Characterization of diffuse axonal pathology and selective hippocampal damage following inertial brain trauma in the pig. *Journal of Neuropathology & Experimental Neurology* 56**,** 822-834.

Souli, M.H., Ouahsine, A., and Lewin, L. (2000). ALE formulation for fluid–structure interaction problems. *Computer methods in applied mechanics and engineering* 190**,** 659-675.

Takhounts, E.G., Ridella, S.A., Hasija, V., Tannous, R.E., Campbell, J.Q., Malone, D., Danelson, K., Stitzel, J., Rowson, S., and Duma, S. (2008). Investigation of traumatic brain injuries using the next generation of simulated injury monitor (SIMon) finite element head model. *Stapp Car Crash Journal* 52**,** 1-31.

Trotta, A., Clark, J.M., Mcgoldrick, A., Gilchrist, M.D., and Annaidh, A.N. (2020). Biofidelic finite element modelling of brain trauma: Importance of the scalp in simulating head impact. *International Journal of Mechanical Sciences* 173**,** 105448.

van Leer, B. (1979). Towards the ultimate conservative difference scheme. V. A second-order sequel to Godunov's method. *Journal of computational Physics* 32**,** 101-136.

Van Noort, R., Black, M., Martin, T., and Meanley, S. (1981). A study of the uniaxial mechanical properties of human dura mater preserved in glycerol. *Biomaterials* 2**,** 41-45.

Van Petten, C. (2004). Relationship between hippocampal volume and memory ability in healthy individuals across the lifespan: review and meta-analysis. *Neuropsychologia* 42**,** 1394-1413.

Viano, D.C., Casson, I.R., Pellman, E.J., Zhang, L., King, A.I., and Yang, K.H. (2005). Concussion in professional football: brain responses by finite element analysis: part 9. *Neurosurgery* 57**,** 891-916.

Wisse, L.E., Biessels, G.J., and Geerlings, M.I. (2014). A critical appraisal of the hippocampal subfield segmentation package in FreeSurfer. *Frontiers in aging neuroscience* 6**,** 261.

Wisse, L.E., Chételat, G., Daugherty, A.M., De Flores, R., La Joie, R., Mueller, S.G., Stark, C.E., Wang, L., Yushkevich, P.A., and Berron, D. (2021). Hippocampal subfield volumetry from structural isotropic 1 mm3 MRI scans: A note of caution. *Human brain mapping* 42**,** 539-550.

Wolf, J.A., Johnson, B.N., Johnson, V.E., Putt, M.E., Browne, K.D., Mietus, C.J., Brown, D.P., Wofford, K.L., Smith, D.H., and Grady, M.S. (2017). Concussion induces hippocampal circuitry disruption in swine. *Journal of neurotrauma* 34**,** 2303-2314.

Yushkevich, P.A., Amaral, R.S., Augustinack, J.C., Bender, A.R., Bernstein, J.D., Boccardi, M., Bocchetta, M., Burggren, A.C., Carr, V.A., and Chakravarty, M.M. (2015). Quantitative comparison of 21 protocols for labeling hippocampal subfields and parahippocampal

subregions in in vivo MRI: towards a harmonized segmentation protocol. *Neuroimage* 111, 526-541.

Zhao, W., Cai, Y., Li, Z., and Ji, S. (2017). Injury prediction and vulnerability assessment using strain and susceptibility measures of the deep white matter. *Biomechanics and modeling in mechanobiology* 16, 1709-1727.

Zhao, W., and Ji, S. (2019). Mesh convergence behavior and the effect of element integration of a human head injury model. *Annals of biomedical engineering* 47, 475-486.

Zhou, Z. (2019). *Evaluation of Fluid-Structure Interaction and Biofidelity of Finite Element Head Models.* Doctor, KTH Royal Institute of Technology.

Zhou, Z., Domel, A.G., Li, X., Grant, G., Kleiven, S., Camarillo, D., and Zeineh, M. (2021a). White matter tract-oriented deformation is dependent on real-time axonal fiber orientation. *Journal of neurotrauma* 38, 1730-1745.

Zhou, Z., Jiang, B., Cao, L., Zhu, F., Mao, H., and Yang, K.H. (2016). Numerical simulations of the 10-year-old head response in drop impacts and compression tests. *computer methods and programs in biomedicine* 131, 13-25.

Zhou, Z., Li, X., and Kleiven, S. (2019a). Biomechanics of acute subdural hematoma in the elderly: A fluid-structure interaction study. *Journal of neurotrauma* 36, 2099-2108.

Zhou, Z., Li, X., and Kleiven, S. (2019b). Fluid–structure interaction simulation of the brain–skull interface for acute subdural haematoma prediction. *Biomechanics and modeling in mechanobiology* 18, 155-173.

Zhou, Z., Li, X., and Kleiven, S. (2020a). Biomechanics of periventricular injury. *Journal of neurotrauma* 37, 1074-1090.

Zhou, Z., Li, X., and Kleiven, S. (2020b). Evaluation of brain-skull interface modelling approaches on the prediction of acute subdural hematoma in the elderly. *Journal of biomechanics* 105, 109787.

Zhou, Z., Li, X., Kleiven, S., and Hardy, W. (2019c). Brain Strain from Motion of Sparse Markers. *Stapp car Crash Journal* 63, 1-27.

Zhou, Z., Li, X., Liu, Y., Fahlstedt, M., Georgiadis, M., Zhan, X., Raymond, S.J., Grant, G., Kleiven, S., and Camarillo, D. (2021b). Towards a comprehensive delineation of white matter tract-related deformation. *Journal of neurotrauma*, ahead of print. http://doi.org/10.1089/neu.2021.0195.

Appendix A: Development of finite element head model without the temporal horn

The finite element (FE) head model without the temporal horn (i.e., the no-temporal-horn (NTH)-Model) used in this study was previously established at KTH Royal Institute of Technology in Stockholm, Sweden (Zhou et al., 2020a). The geometry of the head model was extracted from an averaged magnetic resonance imaging (MRI) head template database (Fillmore et al., 2015). High-resolution T1- and T2-weighted images were segmented using the Freesurfer 7 (Fischl, 2012). The segmentation was subsequently processed by the 3D Slicer (Pieper et al., 2004) to obtain the surfaces of the skull, the brain, the third and the lateral ventricles, with the temporal horn being disregarded. All surfaces then served as an input to the Hexotic software, generating all hexahedron

906 elements based on an octree algorithm (Maréchal, 2009). The falx and tentorium, which were

907 almost invisible in the MRI, were manually created as shell elements based on the anatomical

908 illustrations, while the pia mater and dura mater were generated by finding the outer faces of brain

909 elements and subarachnoid cerebrospinal fluid (CSF) elements, respectively.

910   The material representation of simulated head components is summarized in Table A1 and

911 Table A2. For the brain, a second-order Ogden-based hyperelastic constitutive law was used to

912 describe the nonlinear behavior of the brain tissue, with additional linear viscoelastic terms to

913 account for rate dependence. The subarachnoid CSF was modeled as a nearly incompressible

914 material and shared interfacial nodes with the brain and skull. Mechanical properties of the

915 intracranial membrane (i.e., pia mater and falx/tentorium/dura mater) were determined from the

916 averaged material stress-strain curves from the tissue experiments. The brain, subarachnoid CSF,

917 and intracranial membranes were modeled as Lagrangian elements (Zhou et al., 2020a). In

918 particular, the ventricles were represented by arbitrary Lagrange-Eulerian (ALE) fluid elements,

919 and their responses were coupled to the brain via a fluid-structure interaction (FSI) scheme, which

920 is detailed in the "Cerebral ventricle modeling" and "Brain-ventricle interface modeling" sections

921 of the current study. Note that, in the NTH-model, the temporal horn was substituted as brain

922 parenchyma with the material constants in Table A2.

923 **Table A1. Material properties for the finite element head model.** K is Bulk modulus and N/A
924 is not applicable.

Tissue	Young's modulus (MPa)	Density (kg/dm3)	Poisson's ratio	Reference
Cortical bone	15000	2.00	0.22	(Kleiven, 2007)
Porous bone	1000	1.3	0.24	(Kleiven, 2007)
Brain	Hyper-Viscoelastic (Table A2)	1.04	0.5	(Kleiven, 2007)
CSF/Ventricle	K = 2.1 GPa	1.00	N/A	(Kleiven, 2007)
Dura/Falx/Tentorium	Average stress-strain curve	1.13	N/A	(Aimedieu and Grebe, 2004)
Pia	Average stress-strain curve	1.13	N/A	(Van Noort et al., 1981)

37

925 **Table A2. Ogden hyperelastic and liner viscoelastic constants for the brain material modeling.**
926 μ_i and α_i are Ogden parameters, G_i represents the 6 shear relaxation moduli, β_i are the 6 decay
927 constants.

Parameter	Value	Parameter	Value
μ_1 (Pa)	53.8	α_1	10.1
μ_2 (Pa)	-120.4	α_2	-12.9
G_1 (MPa)	0.32	β_1 (s^{-1})	10^6
G_2 (kPa)	78	β_2 (s^{-1})	10^5
G_3 (kPa)	6.2	β_3 (s^{-1})	10^4
G_4 (kPa)	8.0	β_4 (s^{-1})	10^3
G_5 (kPa)	1.0	β_5 (s^{-1})	10^2
G_6 (kPa)	3.0	β_6 (s^{-1})	10^1

928 **Appendix B: Validation of brain-skull relative motion and brain strain**

929   The strain response and brain-skull relative motion estimated by the model with the

930 temporal horn (i.e., the TH-Model) was validated against the available experimental data presented

931 by Hardy et al. (2007) and Zhou et al. (2019c). In Hardy et al. (2007), a high-speed, biplane X-ray

932 system was used to track the motion of the radiopaque neutral density targets (NDTs) implanted in

933 cluster array within the cadaveric brain. The NDT initial coordinates and motion were obtained

934 with respect to an anatomical coordinate system with the c.g. of the head being the origin. Strain in

935 the volume encompassed by the NDT cluster was calculated by imposing the experimentally

936 measured NDT motions to an auxiliary model that was developed by connecting each NDT to its

937 neighboring counterparts to form tetra elements (Zhou et al., 2019c).

938   In the present work, three representative cases are selected, including C288-T3 (sagittal

939 impact), C380-T1 (coronal impact), and C380-T2 (horizontal impact). To numerically reproduce

940 the experimental impacts, the recorded head kinematic curves were imposed to the node which

941 locates at the center of gravity of the corresponding cadaveric head and is rigidly attached to the

942 skull. To approximate the specimen anthropometry, the model was scaled independently in

943 directions of both the depth and breadth to match the reported cadaveric head sizes. The node

944 nearest to the start position of an experimental NDT target was taken as the marker location in the

945 model. Motions of the identified nodes with respect to the skull along three anatomical coordinate

946 directions are obtained from the whole head model simulation with the detailed results presented in

38

947 **Fig. B1-B3**. Following the procedures established by Zhou et al. (2019c), the initial positions of the

948 identified nodes and the nodal motion responses predicted in the model was used to calculate the

949 strain responses, specifically first principal Green-Lagrange strain and shear Green-Lagrange strain,

950 of the brain model. The strain validation results are shown in **Fig. B4.**
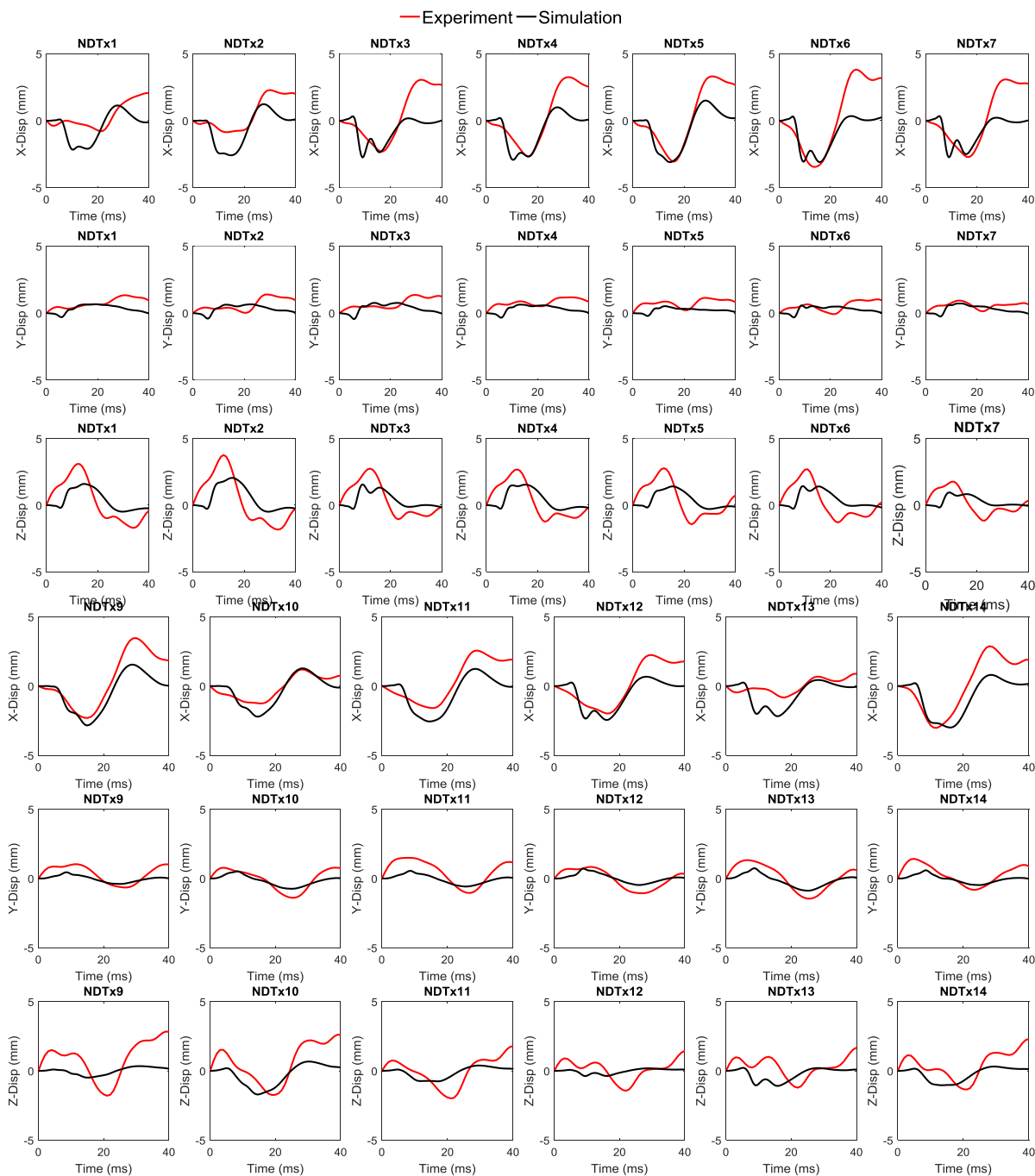
951
952 **Fig B1. Comparison between experimental and simulated brain-skull relative motion for the**
953 **experiment C288-T3.**
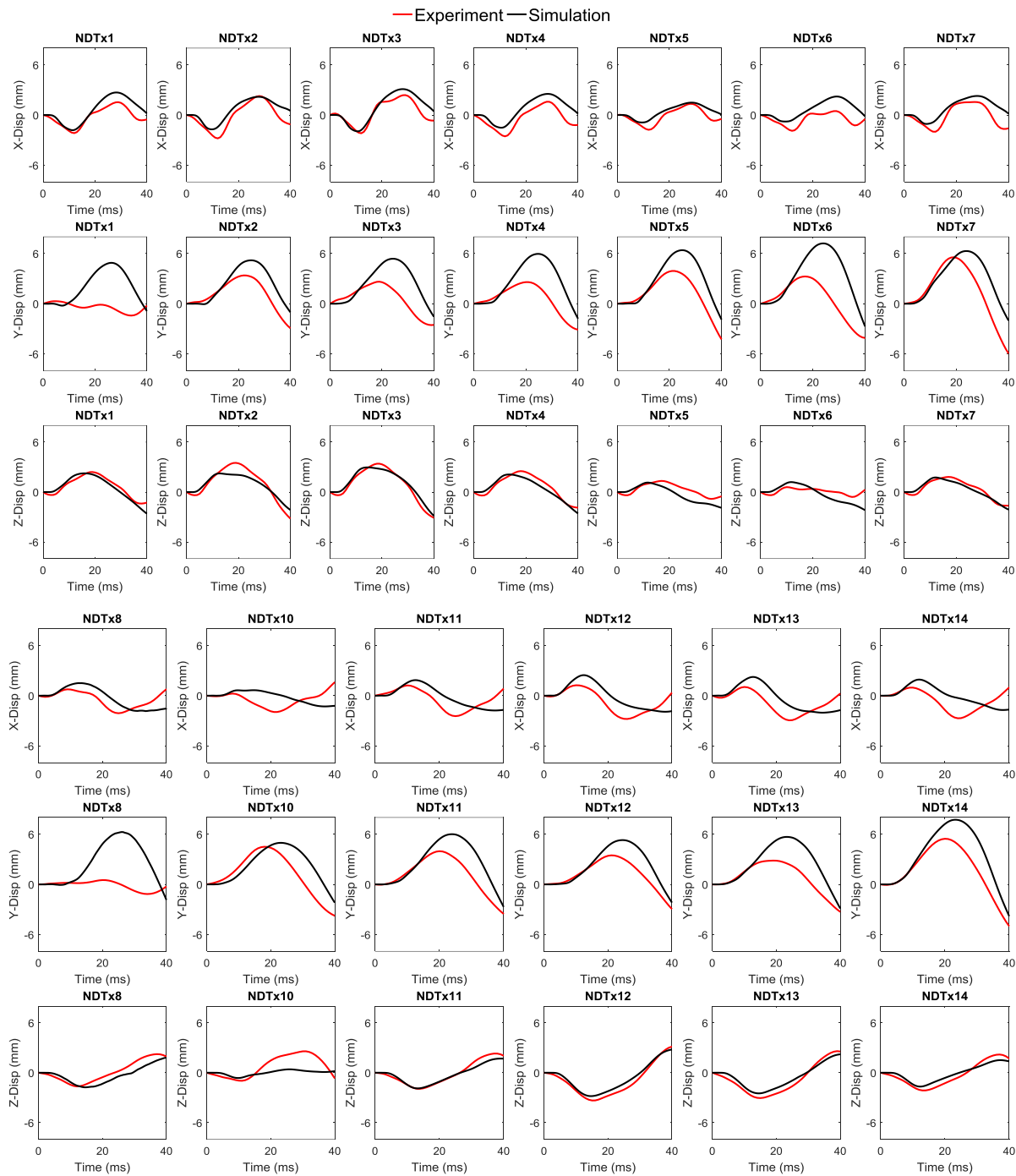
Fig B1. Comparison between experimental and simulated brain-skull relative motion for the experiment C380-T1.
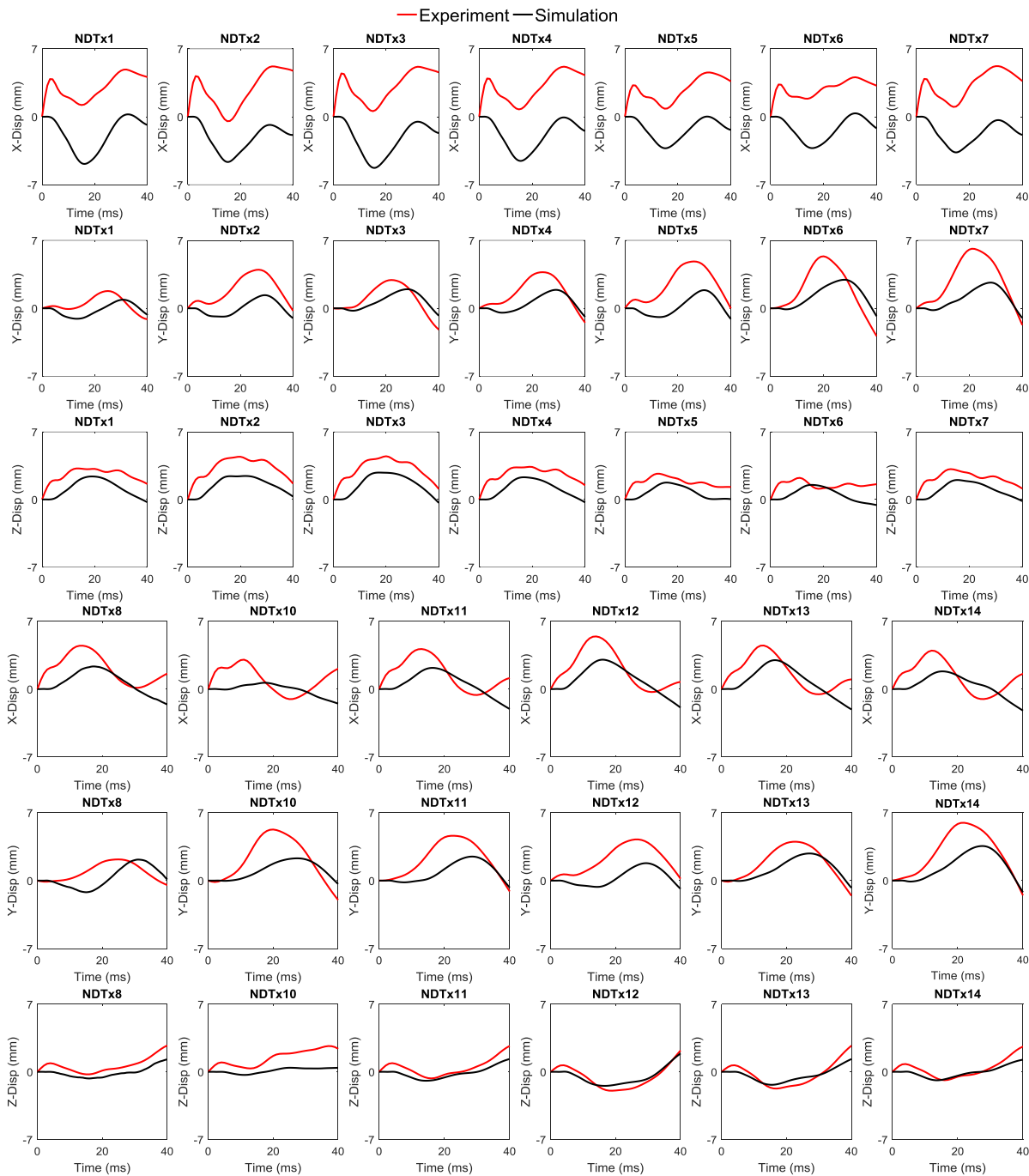
Fig B3. Comparison between experimental and simulated brain-skull relative motion for the experiment C380-T2.
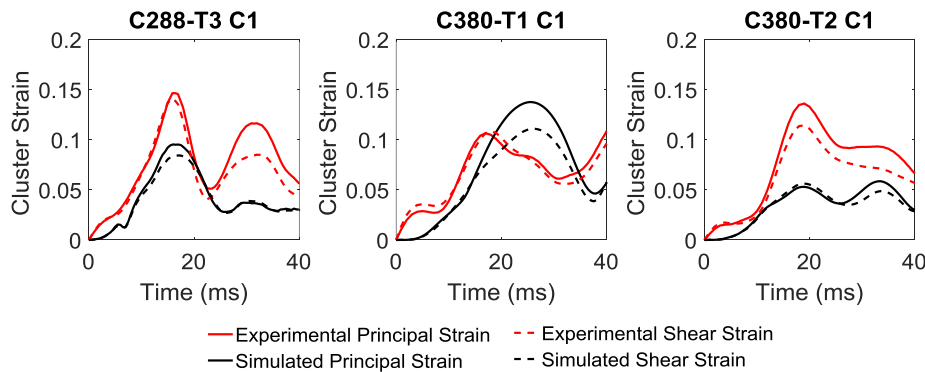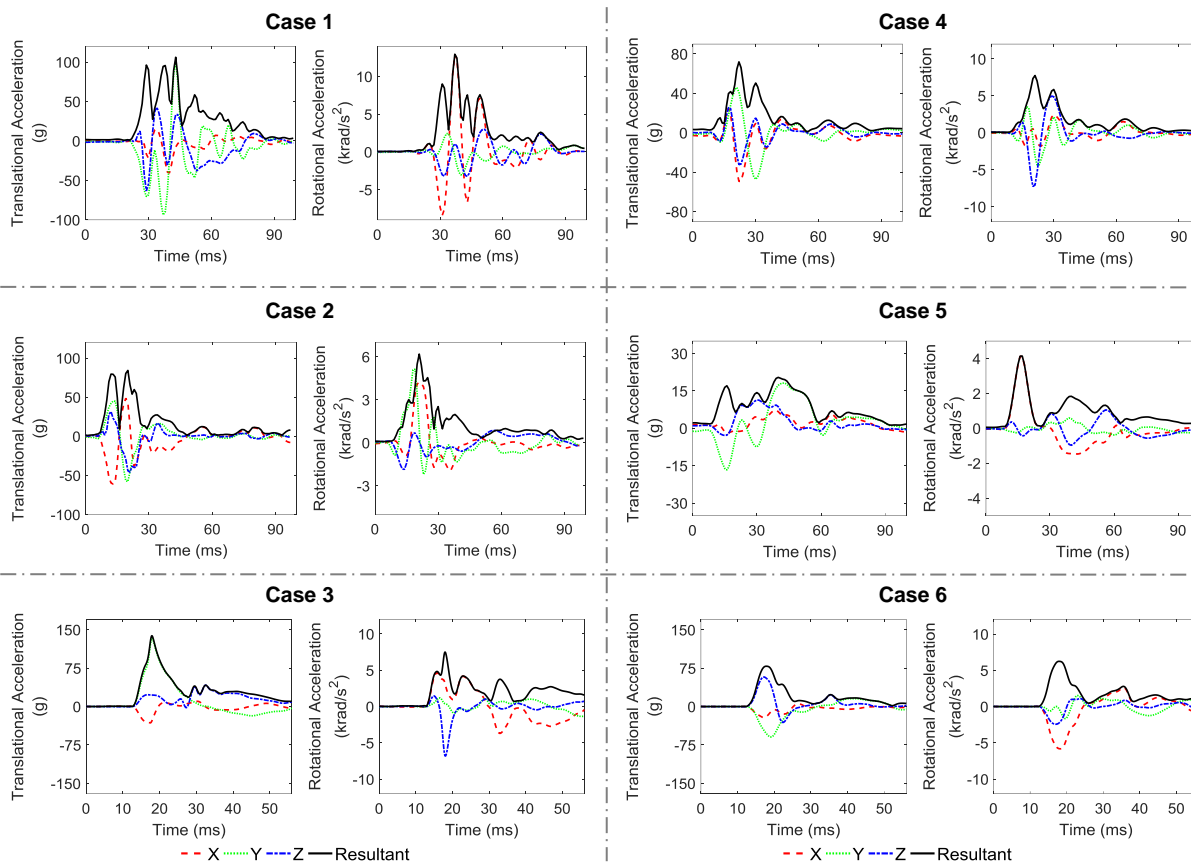
961 **Fig B4. Comparison between experimental and simulated brain strains.**

962 **Appendix C: Loading curves for 3 concussive impacts and 3 sub-concussive impacts**

963

964 **Fig C1. Loading conditions for 3 concussive impacts (Cases 1-3) and 3 sub-concussive impacts**
965 **(Cases 4-6).** The X, Y, and Z axes are the same as those in the skull-fixed coordinate system in Fig.
966 1a.

967 **Appendix D: Volume ratio of the hippocampal subfields and whole hippocampus with strain**
968 **over 0.2 and strain rate over 30 s^{-1}**
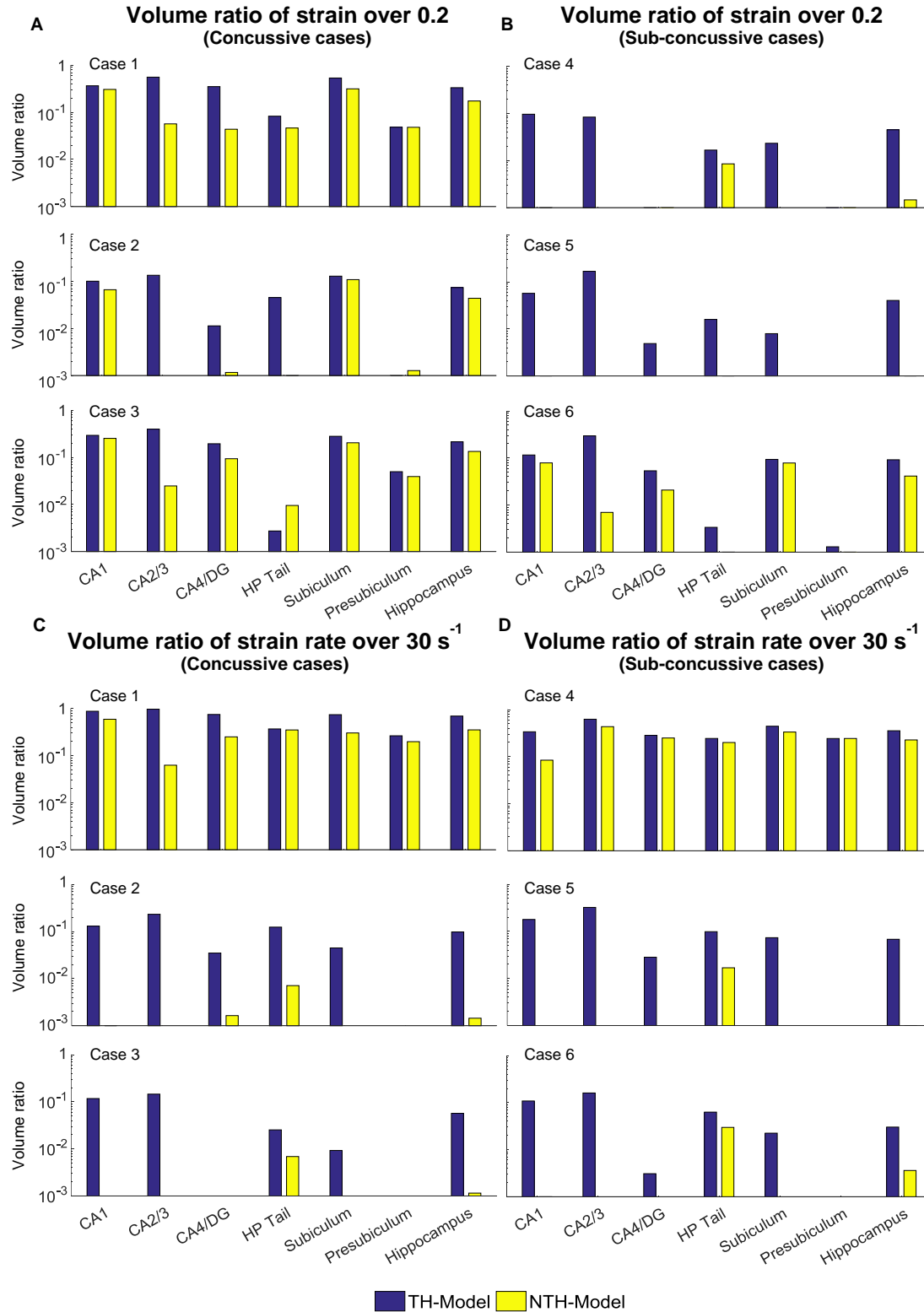
Hippocampus

Fig. D1. Volume ratio of the maximum principle strain over 0.2 and strain rate over 30 s^{-1} in the hippocampal subfields and the whole hippocampus between the TH-Model and NTH-model of 3 concussive impacts (Cases 1-3) and 3 sub-concussive impacts (Cases 4-6).

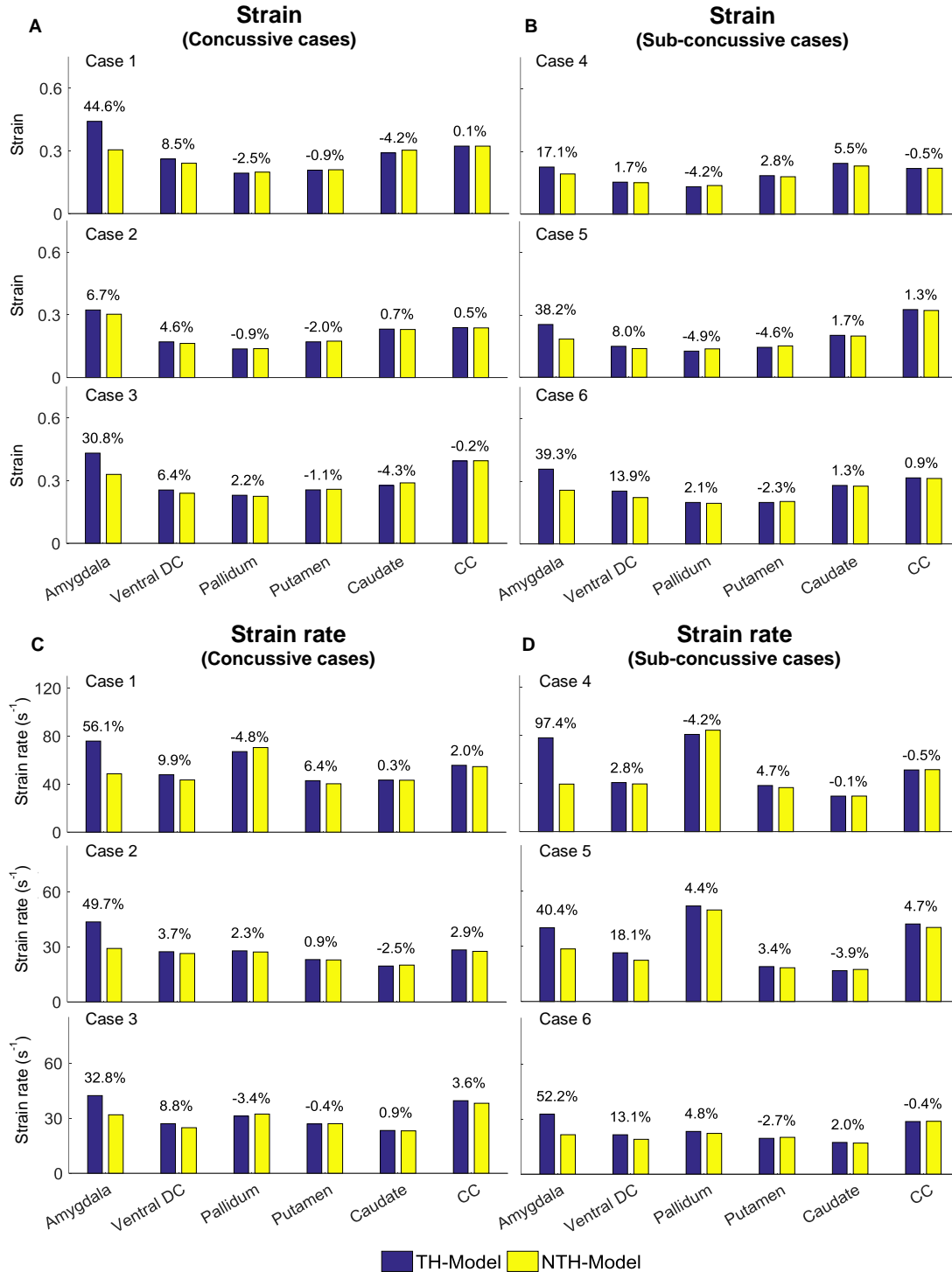**Appendix E: Comparison of strain and strain rate in the non-hippocampal regions**

Fig E1. Comparison of strain and strain rate in the non-hippocampal regions between the TH-model and NTH-model of 3 concussive impacts (Cases 1-3) and 3 sub-concussive impacts (Cases 4-6). (A) Comparison of strain in the non-hippocampal periventricular regions of 3 concussive impacts. (B) Comparison of strain in the non-hippocampal periventricular regions of 3 sub-concussive impacts. (C) Comparison of strain rate in the non-hippocampal periventricular regions of 3 concussive impacts. (D) Comparison of strain rate in the non-hippocampal periventricular regions of 3 sub-concussive impacts. Percentages in strain difference and strain rate difference are calculated with the results of the NTH-model as the baseline. Ventral DC: ventral diencephalon; CC: Corpus callosum.